J. Fluid Mech. (2010), *vol.* 659, *pp.* 289–317.
doi:10.1017/S002211201000248X

Breaking of shoaling internal solitary waves

PAYAM AGHSAEE[1], LEON BOEGMAN[1]† AND KEVIN G. LAMB[2]

[1]Department of Civil Engineering, Queen's University, Kingston, Ontario K7L 3N6, Canada

[2]Department of Applied Mathematics, University of Waterloo, Ontario N2L 3G1, Canada

(Received 24 September 2009; revised 21 April 2010; accepted 22 April 2010; first published online 15 July 2010)

The breaking of fully nonlinear internal solitary waves of depression shoaling upon a uniformly sloping boundary in a smoothed two-layer density field was investigated using high-resolution two-dimensional simulations. Our simulations were limited to narrow-crested waves, which are more common than broad-crested waves in geophysical flows. The simulations were performed for a wide range of boundary slopes $S \in [0.01, 0.3]$ and wave slopes extending the parameter range to weaker slopes than considered in previous laboratory and numerical studies. Over steep slopes ($S \geqslant 0.1$), three distinct breaking processes were observed: surging, plunging and collapsing breakers which are associated with reflection, convective instability and boundary-layer separation, respectively. Over mild slopes ($S \leqslant 0.05$), nonlinearity varies gradually and the wave fissions into a train of waves of elevation as it passes through the turning point where solitary waves reverse polarity. The dynamics of each breaker type were investigated and the predominance of a particular mechanism was associated with a relative developmental time scale. The breaking location was modelled as a function of wave amplitude (a), characteristic wave length and the isopycnal length along the slope. The breaker type was characterized in wave slope ($S_w = a/L_w$, where L_w is a measure of half of the wavelength) versus S space, and the reflection coefficient (R), modelled as a function of the internal Iribarren number, was in agreement with other studies. The effects of grid resolution and wave Reynolds number (Re_w) on R, boundary-layer separation and the evolution of global instability were studied. High Reynolds numbers ($Re_w \sim 10^4$) were found to trigger a global instability, which modifies the breaking process relative to the lower Re_w case, but not necessarily the breaking location, and results in a $\sim 10\,\%$ increase in R, relative to the $Re_w \sim 10^3$ case.

Key words: internal waves, stratified flows, topographic effects

1. Introduction

Internal solitary waves (ISWs) are formed via the nonlinear steepening of basin-scale internal seiches in lakes (Horn, Imberger & Ivey 2001) and from the internal tide generated by tide–topography interaction in oceans (Apel *et al.* 1985; Lamb 1994). The breaking of ISWs upon sloping boundaries in lakes and oceans plays an important role in controlling the stratification and vertical distribution of biogeochemical matters in the water column (Ledwell & Hickey 1995; Wüest, Piepke & Van Senden 2000) as

† Email address for correspondence: leon.boegman@civil.queensu.ca

well as the dissipation of internal wave energy (Imberger 1998; Michallet & Ivey 1999; Boegman, Ivey & Imberger 2005). Field experiments in lakes have shown that the dissipation and diapycnal diffusivity in the turbulent benthic boundary layer (TBBL), where internal solitary waves break, are an order of magnitude greater than in the lake interior (Imberger 1998; Wüest *et al.* 2000). Laboratory experiments have shown that as much as 25 % of the basin-scale seiche energy is transferred to an ISW packet (Boegman *et al.* 2005), which in turn can lose up to 90 % of its energy to mixing and dissipation via breaking upon a sloping boundary (Helfrich 1992; Michallet & Ivey 1999). Shoaling of ISWs over sloping regions can also lead to sediment resuspension due to vortex formation at the toe of the wave (Hosegood, Bonnin & van Haren 2004; Bogucki, Redekopp & Barth 2005; Boegman & Ivey 2009). Nutrient-rich suspended sediments will subsequently intrude towards the lake interior (Thorpe 1998; Marti & Imberger 2004).

Field experiments on ISW breaking have been limited due to difficulties in predicting the breaking location and obtaining high spatial and temporal resolution data (e.g. Moum *et al.* 2003; Orr & Mignerey 2003). Consequently, laboratory experiments (e.g. Kao, Pan & Renouard 1985; Helfrich 1992; Michallet & Ivey 1999; Boegman *et al.* 2005) and numerical simulations (e.g. Lamb 2002; Vlasenko & Hutter 2002; Bourgault *et al.* 2007; Lamb & Nguyen 2009) have been extensively performed to study the shoaling mechanisms of internal solitary waves. In these studies, two particular shoaling mechanisms have been observed. Over mild slopes, fission occurs after the polarity reversal at the turning point and there is little reflection (e.g. Helfrich, Melville & Miles 1984; Orr & Mignerey 2003; Shroyer, Moum & Nash 2009). Over steep slopes, wave breaking occurs where some wave energy is irreversibly lost to dissipation and diapycnal mixing, while the remainder is reflected from the slope (e.g. Michallet & Ivey 1999; Boegman *et al.* 2005; Bourgault & Kelley 2007). Wave breaking has been observed to occur through shear instability (e.g. Kelvin–Helmhotz instability; Kao *et al.* 1985; Moum *et al.* 2003; Boegman *et al.* 2005) and Rayleigh–Taylor gravitational instability (Helfrich & Melville 1986; Michallet & Ivey 1999; Vlasenko & Hutter 2002).

The ISW breaking mechanism has been further classified by analogy to surface breakers according to an internal form of the Iribarren number

$$\xi_{in} = \frac{S}{\sqrt{a/L_w}}, \tag{1.1}$$

where S, a and L_w represent boundary slope, wave amplitude (taken positive for waves of depression) and wavelength, respectively (Boegman *et al.* 2005). The internal Iribarren number could delineate spilling, plunging and collapsing breakers in the laboratory experiments of Boegman *et al.* (2005); however, their experiments were limited to a small range of steep boundary slopes (0.1–0.15) permissible with their experimental set-up. These are much steeper than those found in lakes (0.01) and coastal oceans (0.001); thus, they were not able to observe the fission process.

In those experiments, the breaking mechanism was influenced by the space–time variable background flow resulting from basin-scale seiche oscillations. In lakes and oceans the ratio of the horizontal to vertical length scales is much larger than that in the laboratory, which causes the period of basin-scale motions to be 100–1000 times greater than the time scale associated with ISW shoaling (Imberger 1998). Basin-scale motions will be frozen in time during ISW shoaling and can consequently be neglected when considering ISW shoaling (e.g. Helfrich 1992; Michallet & Ivey 1999).

Field observations suggest that resuspension related to shoaling of ISWs is due to flow separation beneath the ISWs (e.g. Bogucki *et al.* 2005). This process has been well studied numerically and experimentally for the case of ISW travelling over a flat bottom (e.g. Bogucki & Redekopp 1999; Diamessis & Redekopp 2006; Carr, Davies & Shivaram 2008; Stastna & Lamb 2008) where flow separation has been found to be dependent upon the Reynolds number ($Re = Hc_0/\nu$; Diamessis & Redekopp 2006). Here H, c_0 and ν represent total depth, linear phase speed and fluid viscosity, respectively. Process-oriented studies on resuspension and separation on sloping topography have been limited (Boegman & Ivey 2009) and Re effects have not been investigated.

The reflection coefficient (R) is often employed to determine energy loss in the littoral zone from offshore observations (e.g. Michallet & Ivey 1999; Boegman *et al.* 2005). However, parameterizations for R are not in agreement (Helfrich 1992; Michallet & Ivey 1999). This may be because of sidewall effects in the laboratory (Bourgault & Kelley 2007) or because they assume an equipartition between the potential and kinetic energies of the wave or an equipartition of their fluxes. Lamb & Nguyen (2009) showed that equipartition is only reasonable for weakly nonlinear waves and that for highly nonlinear waves there may be up to 30 % more kinetic energy than potential energy in the wave. Moreover, the potential energy flux can be up to five times the kinetic energy flux. There is a need to recalculate the parameterizations for R without assuming an energy/energy flux equipartition.

In the present study, we extend the work described above by performing high-resolution two-dimensional simulations of ISWs of depression shoaling upon closed slopes in a smoothed two-layer density field. The objectives of our study are as follows. To investigate the validity of the Iribarren model for internal wave breaking over a greater range of wave and boundary slopes in a quiescent ambient flow, to determine the effects of Re on wave breaking and flow separation and to test the parameterizations for R by directly calculating the kinetic and potential energy fluxes. In § 2 we present the relevant theoretical background. We introduce the numerical model and methodology in § 3. The results and their physical interpretation are given in § 4. The breaking criteria, breaking location, effects of Re and models for R are discussed in § 5, followed by concluding remarks in § 6.

2. Theoretical background

Stratified lakes and oceans with a thin pycnocline relative to the total depth H may be approximated as a two-layer system of depth h_1 and density ρ_1 overlaying depth h_2 and density ρ_2 where $H = h_1 + h_2$ (figure 1). The generation and propagation of ISWs in this two-layer system can be theoretically analysed using the Korteweg–de Vries (KdV) equation (Osborne & Burch 1980; Apel 2002):

$$\eta_t + c_0\eta_x + \alpha\eta\eta_x + \beta\eta_{xxx} = 0, \tag{2.1}$$

$$\alpha = \frac{3c_0}{2}\frac{h_1 - h_2}{h_1 h_2}\ \beta = \frac{c_0}{6}h_1 h_2, \tag{2.2}$$

which is derived by applying first-order perturbation techniques on the hydrodynamic equations for an inviscid fluid under the Boussinesq approximation. Here η is the vertical displacement of the pycnocline. The KdV equation models weakly nonlinear, weakly dispersive waves which, for the case of internal waves in a two-layer fluid, has nonlinearity and dispersion coefficients (α and β respectively) in the form of (2.2). Here $c_0 = \sqrt{g'h_1h_2/(h_1 + h_2)}$ is the linear long-wave speed where under the Boussinesq

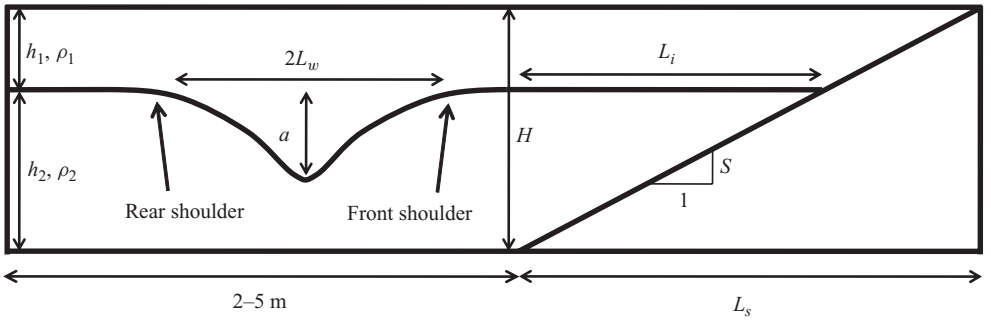

FIGURE 1. Schematic picture of numerical simulations. Here H is the total depth where fluid of density ρ_1 and depth h_1 overlies fluid of density ρ_2 and depth h_2. An internal solitary wave of amplitude a and length $2L_w$ moves towards the boundary that has slope S. The interface length above the slope is L_i, and L_s is the horizontal length of the slope.

approximation, $g' = g(\rho_2 - \rho_1)/\rho_2$ is the reduced gravity due to stratification. The horizontal length scale of a KdV solitary wave can be expressed as

$$\lambda = \sqrt{\frac{12\beta}{|\alpha|\, a}}. \tag{2.3}$$

The third term of (2.1) is the nonlinear term responsible for nonlinear steepening, which for a solitary wave is balanced by the fourth term, the dispersive term. To unify the effects of both finite wave amplitude and asymmetry of the layer thicknesses on ISW nonlinearity, Boegman *et al.* (2005) proposed the non-dimensional nonlinearity parameter

$$\gamma = \frac{|\alpha|\, a}{c_0} = \frac{3}{2} a \frac{|h_1 - h_2|}{h_1 h_2}. \tag{2.4}$$

In geophysical flows, typically $h_1 < h_2$ causing α to be negative and leading to the generation of ISWs of depression (figure 1). During the passage of a wave of depression, fluid particles in the upper and lower layers will move in the same and opposite direction to wave propagation, respectively.

By keeping only first-order nonlinear terms in its derivation, the KdV equation is only valid when the wave amplitude is much smaller than $(h_2 - h_1)/2$ (Lamb & Wan 1998). Solitary wave solutions of the KdV equation are unbounded in amplitude and the wavelength decreases with amplitude. Numerical solutions of the fully nonlinear equations under the Boussinesq approximation show that solitary wave amplitudes are bounded by $a_{max} = (h_2 - h_1)/2$ for a two-layer fluid (Lamb & Wan 1998). This indicates that broadening starts when the interface approaches the mid-depth of the water column.

The nonlinearity parameter γ captures the effects of the two nonlinear length scales h_1/H and a/h_1 defined by Horn *et al.* (2001). The above-mentioned maximum amplitude criterion may be presented in terms of these length scales as

$$\frac{a}{h_1} < \frac{0.5}{\left(\dfrac{h_1}{H}\right)} - 1 \tag{2.5}$$

to determine the geophysical parameter range over which narrow-crested and broad-crested waves are expected. The curved line in figure 2 demonstrates (2.5), where the

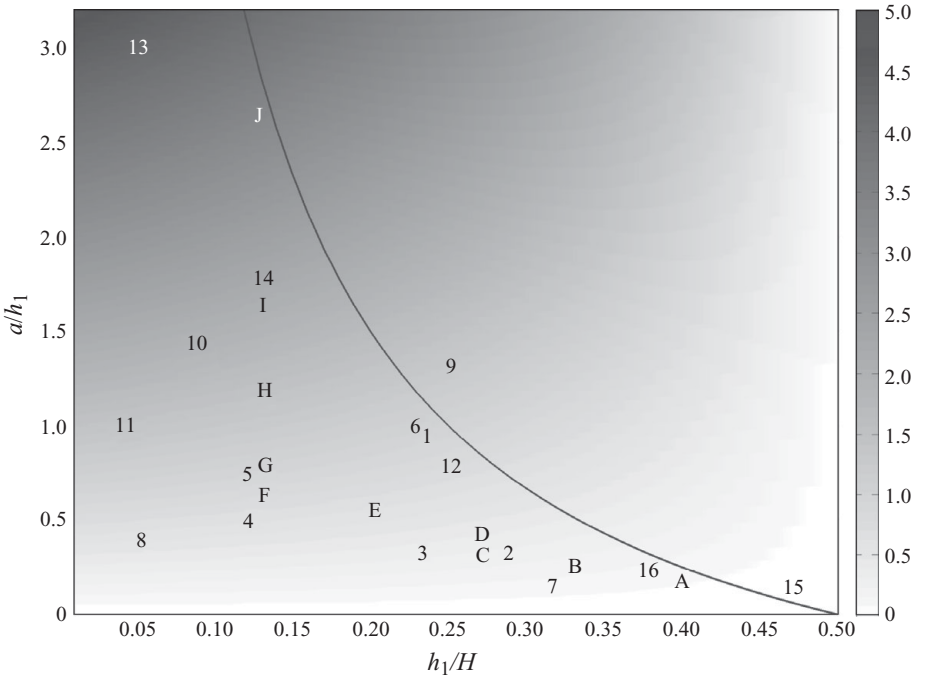

FIGURE 2. Nonlinearity parameter (γ) shaded in greyscale as a function of h_1/H and a/h_1. The area above the curved line represents broad-crested waves while narrow-crested waves lie below it. Capital letters (A to J) represent the waves generated in our simulations with details in table 1. Numbers show the waves observed in field studies: 1, Lake Biwa; 2, Lake Pusiano; 3, Loch Ness; 4 and 5, Babine Lake; 6, Seneca Lake; 7, Kootenay Lake; 8, Sulu Sea; 9, Scotian Shelf; 10, Massachusetts Bay; 11, Strait of Gibraltar; 12, Bodensee; 13, Oregon shelf; 14, St Lawrence; 15 and 16, Lake Kinneret (data taken from Boegman *et al.* 2005).

waves above this line have amplitudes larger than $(h_2 - h_1)/2$ thus have broad crests. Sixteen waves from the literature with sufficient data are plotted in figure 2. The majority of these waves, from both lakes and oceans, have narrow crests. However, this is a tiny fraction of the reported 3581 internal solitary waves observed in the world oceans over a 21 month period (Jackson 2007). It should be noted that in the field there may be background currents which modifies maximum wave amplitude. For example, the Scotian shelf case (wave number 9) could possibly be below the curved line if background currents were taken into account. The nonlinearity parameter γ may also be expressed as an explicit function of h_1/H and a/h_1

$$\gamma = \frac{3}{2}\frac{a}{h_1}\frac{\left|1 - 2\dfrac{h_1}{H}\right|}{1 - \dfrac{h_1}{H}} \tag{2.6}$$

showing how γ captures the degree of nonlinearity throughout the h_1/H versus a/h_1 domain. Figure 2 where 7 is shown in the shaded region indicates that we may investigate narrow-crest ISWs of depression over the range $0.1 < \gamma < 3$ to sufficiently cover what is found in nature.

3. Numerical model and experimental parameters

The simulations were performed using a two-dimensional nonlinear non-hydrostatic computational fluid dynamics model (Lamb & Nguyen 2009). The model solves the Navier–Stokes equations for a Newtonian fluid with the Boussinesq approximation

$$\frac{\partial u}{\partial t} + u\frac{\partial u}{\partial x} + w\frac{\partial u}{\partial z} = -\frac{1}{\rho_0}\frac{\partial P}{\partial x} + \nu\nabla^2 u, \tag{3.1}$$

$$\frac{\partial w}{\partial t} + u\frac{\partial w}{\partial x} + w\frac{\partial w}{\partial z} = -\frac{1}{\rho_0}\frac{\partial P}{\partial z} - \frac{\rho g}{\rho_0} + \nu\nabla^2 w, \tag{3.2}$$

$$\frac{\partial \rho}{\partial t} + u\frac{\partial \rho}{\partial x} + +w\frac{\partial \rho}{\partial z} = k\nabla^2 \rho, \tag{3.3}$$

$$\frac{\partial u}{\partial x} + \frac{\partial w}{\partial z} = 0, \tag{3.4}$$

where (x, z) are the horizontal and vertical coordinates and (u, w) is the associated velocity vector, P and ρ are the pressure and density fields, respectively, ρ_0 is the reference density, ν is the kinematic viscosity and k is molecular diffusivity. A σ-coordinate system is applied allowing for greater vertical resolution over the slope where the depth decreases. A no-slip boundary condition is applied along the bottom and two end walls and a free-slip condition is applied at the rigid lid (Lamb & Nguyen 2009). A no-flux boundary condition has been employed for the density field on all boundaries. The vertical variation in density is given by a *tanh* profile

$$\bar{\rho}(z) = \frac{\rho_1 + \rho_2}{2} - \frac{\rho_2 - \rho_1}{2}\tanh\left(\frac{z - z_{pyc}}{d_{pyc}}\right), \tag{3.5}$$

which approximates a two-layer stratification in the laboratory (Boegman & Ivey 2009). Here the vertical coordinate z varies between zero at the surface to $-H$ at the flat bottom, z_{pyc} is the location of the centre of the pycnocline and d_{pyc} is a measure of half the pycnocline thickness.

There are limitations in modelling a three-dimensional wave-breaking process using a two-dimensional numerical model. Fringer & Street (2003) and Venayagamoorthy & Fringer (2007) showed that three-dimensionality is not evident until after the cross-stream rolls develop as a result of an initial two-dimensional instability. Our two-dimensional model is incapable of reproducing the secondary instabilities, which account for a significant portion of the dissipation in three-dimensional computations (Fringer & Street 2003) and we therefore expect our numerical solution to be physically realistic during only the initial two-dimensional stages of wave instability and breaking (Boegman & Ivey 2009). Mixing and dissipation, which occur primarily during the later stages of breaking, will not be correctly modelled (Lamb, Boegman & Ivey 2005) and consequently these processes are not the focus of this study.

The model is initialized by first solving the Dubreil–Jacotin–Long (DJL) equation derived in terms of streamline displacement (Lamb 2002; (6) therein). For a specified available potential energy, the DJL equation is solved by minimizing the kinetic energy. This generates an incident ISW which propagates along the flat bottom until it shoals upon the sloping boundary at the end of the calculation domain (figure 1). Away from the slope, the horizontal and vertical grid resolutions are 2.5 mm and 1 mm, respectively. At these resolutions the simulations were grid-independent. The diffusivity was 10^{-9} m^2 s^{-1}. To match conditions from prior laboratory experiments (e.g. Michallet & Ivey 1999) the total depth for all simulations was set to $H = 0.15$ m.

							Boundary slope						
							0.01	0.03	0.05	0.1	0.15	0.2	0.3
Wave	h_1 (m)	a (m)	L_w (m)	$\frac{2a}{h_2-h_1}$	γ	d_{pyc} (m)	Simulation number and (type of shoaling process)						
A	0.06	0.012	0.96	0.78	0.10	0.0015	11(F)	22(F)	32(F)	1(S)	62(S)	42(S)	52(S)
B	0.05	0.013	0.65	0.53	0.20	0.0015	12(F)	23(F)	33(F)	2(CS)	63(S)	43(S)	53(S)
C	0.04	0.013	0.45	0.37	0.31	0.0015	13(F)	24(F)	34(F)	3(C)	64(CS)	44(CS)	54(S)
D	0.04	0.016	0.46	0.47	0.39	0.0015	14(F)	25(F)	35(F)	4(C)	65(C)	45(CP)	55(S)
E	0.03	0.017	0.32	0.38	0.63	0.0015	15(F)	26(F)	36(F)	5(C)	66(C)	46(CP)	56(CP)
F	0.02	0.013	0.23	0.24	0.83	0.0015	16(F)	27(F)	37(F)	6(C)	67(C)	47(CP)	57(CP)
G	0.02	0.016	0.22	0.29	1.02	0.0015	17(F)	28(F)	38(F)	7(C)	68(CP)	48(CP)	58(CP)
H	0.02	0.024	0.22	0.44	1.52	0.0015	18(F)	29(F)	39(C)	8(C)	69(CP)	49(P)	59(P)
I	0.02	0.033	0.22	0.60	2.09	0.0025	19(F)	30(C)	40(C)	9(C)	70(P)	50(P)	60(P)
J	0.02	0.041	0.22	0.75	2.60	0.003	20(F)	31(C)	41(C)	10(C)	71(P)	51(P)	61(P)

TABLE 1. Main parameters of performed numerical simulations. The letters in front of simulation numbers represent the shoaling type: F for fission, C for collapsing, S for surging and P for plunging. The wave slope $S_w = a/L_w$, where L_w is a measure of half of the wavelength.

Ten waves were generated with amplitudes between 0.01 and 0.04 m to cover the range $0.1 < \gamma < 3$ (table 1). For all simulations, ρ_1 and ρ_2 were set to 1000 and 1040 kg m^{-3}, respectively. The typical maximum density difference observed over the pycnocline in stratified lakes and oceans is ~ 1 kg m^{-3} (e.g. Boegman *et al.* 2003; Orr & Mignerey 2003). This implies that we are simulating faster propagating waves than would be the case using density values observed in lakes/oceans. This will partially compensate for reducing the Reynolds number by decreasing the physical scale; however, using a density difference 40 times larger than that in lakes and oceans produces a Reynolds number that is equivalent to increasing the water depth by a factor of $\sqrt[3]{40} \approx 3.4$ to a depth of 50 cm so the compensation is extremely small. Moreover, considering density ratios between 1.01 and 1.04, Michallet & Ivey (1999) showed that the breaking characteristics (reflection and mixing efficiency) are insensitive to density difference (their figures 9 and 10). The simulations were performed over a range of slopes from mild (0.01) to steep (0.3) to allow for both fission and convective breaking. The mild slopes are of the same order as those found in lakes, but are greater than coastal ocean slopes. Simulation of oceanic slopes would require prohibitively large computational domains. We have observed that slopes of ~ 0.01 are sufficient to model fission for the range of wave amplitudes considered in this study. The experimental variables considered in this study are given in table 1.

To calculate the Iribarren number, the wavelength is determined through integration of the wave profile (Michallet & Ivey 1999)

$$L_w = \frac{1}{a} \int_{-\infty}^{+\infty} \eta(x)\, \mathrm{d}x, \tag{3.6}$$

where $\eta(x)$ is the vertical displacement, positive downwards, of the isopycnal at the centre of the pycnocline. Our observations show that the actual wavelength is $L \approx 2L_w$ (see figure 1). Thus, we define the wave slope $S_w = a/L_w$, which increases linearly with γ (figure 3) for the simulated narrow-crested ISWs. In addition, the maximum internal wave Froude number ($Fr_{max} = u_{max}/c_0$; Fringer & Street 2003) was seen to increase with γ (figure 3). Here u_{max} is the maximum flow speed within the wave. In our

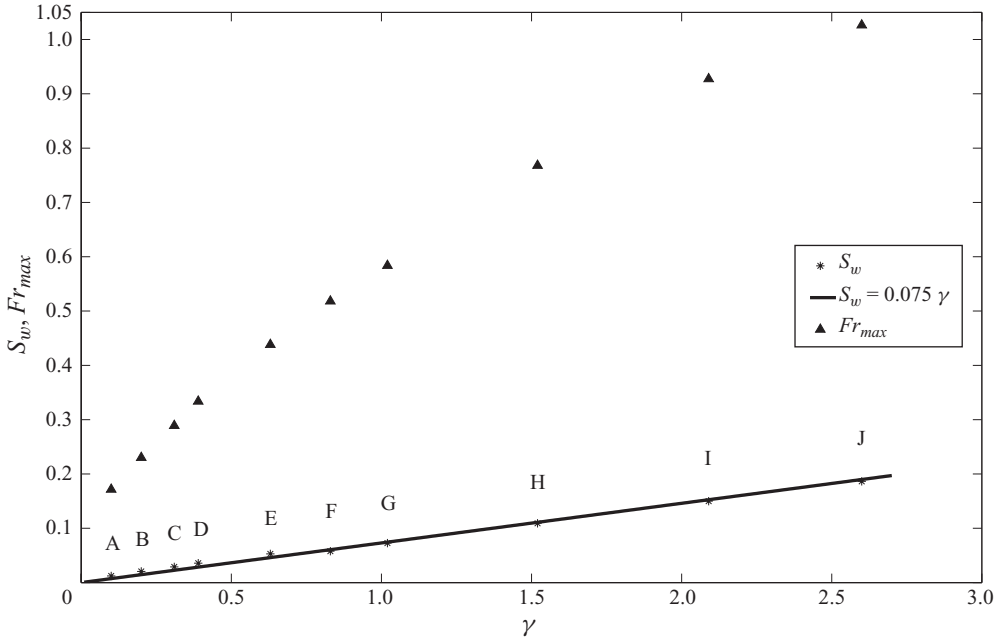

FIGURE 3. Wave front slope (S_w) and the maximum Froude number within the wave (Fr_{max}), versus nonlinearity parameter (γ) for waves in the simulations.

simulations different wave and boundary slopes will interact with each other, thus varying the internal Iribarren number.

4. Results

4.1. *Flow field*

A typical wave shoaling event proceeds as follows. As the wave of depression shoals, the volume of lower layer fluid confined between the leading edge of the wave and the sloping boundary is reduced as the leading face of the wave becomes parallel to the slope. In this region, down-slope velocities are increased due to the fluid escaping beneath the wave trough. The associated lengthening of the leading face and large velocities underneath it generate shear across the interface, leading to the possibility of shear instabilities as have been observed in laboratory experiments (Kao *et al.* 1985; Boegman *et al.* 2005). Shear instabilities were not observed in the present simulations.

The rear face of the wave steepens because the rear shoulder of the wave is in deeper water relative to the wave trough and hence propagates faster. Steepening of the rear face acts to move the location of maximum horizontal velocity from the wave centre to the rear shoulder (figure 4), which can lead to overturning. For some simulations there was an upward motion of the rear face associated with shoaling in addition to the forward steepening. The upward motion forms a positive tail behind the rear face, which gradually increases in amplitude and becomes narrower causing a reversal in the flow direction within the upper layer from onshore to offshore. The positive tail formation can be attributed to the effect of slowly varying nonlinearity (Grimshaw, Pelinovsky & Talipova 1998) and is the main mechanism leading to the fission process. As the nonlinearity varies along the slope, decreasing L_w/L_i (L_i is the

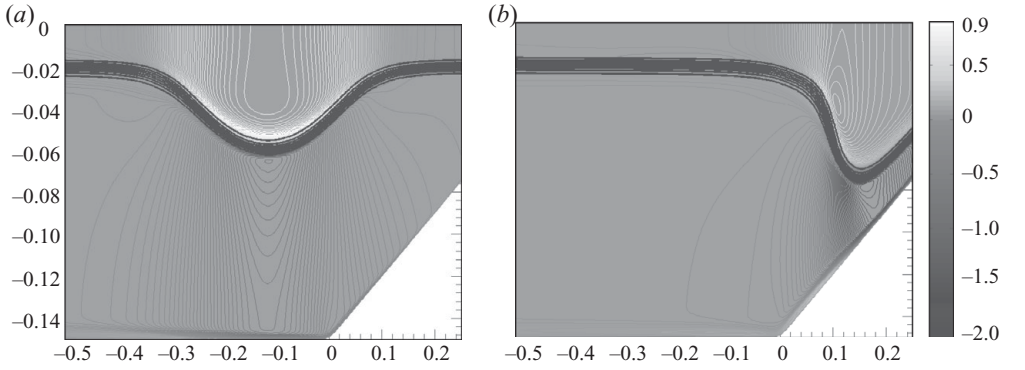

FIGURE 4. Horizontal velocity over linear phase speed (u/c_0) as the wave shoals (simulation 61). Thick black lines are isopycnals and thin contours show horizontal velocity field. Maximum horizontal velocity has shifted from middle of the wave to the rear shoulder.

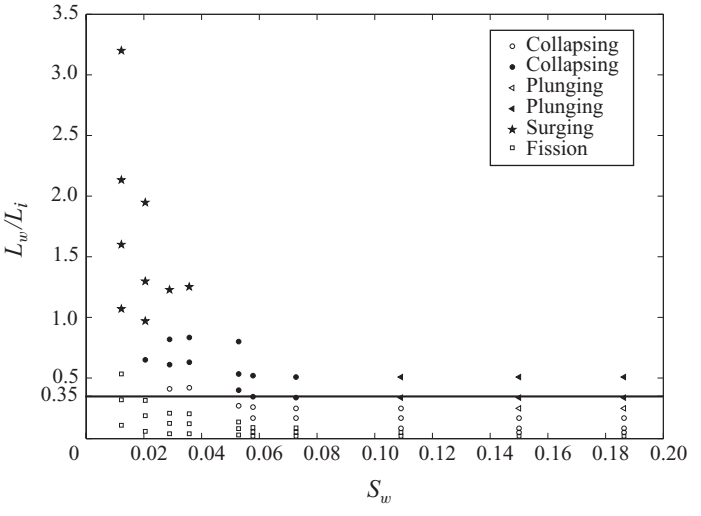

FIGURE 5. A criterion to differentiate the simulations in which a positive tail emerges ($L_w < \sim 0.35L_i$). The hollow symbols represent simulations in which positive tail formation occurred.

pycnocline length above the slope; figure 1) leads to more slowly varying nonlinearity. Our data show that positive tail formation occurs when $L_w < \sim 0.35L_i$ (figure 5).

Separation of the down-slope flow was also observed beneath the shoaling wave. Flow separation occurs in the adverse pressure-gradient region where the flow decelerates after passing beneath the wave trough.

To characterize the different breaking mechanisms, three time scales were measured after the leading edge of the wave reached the toe of the slope. Surging breakers are governed by the time scale for the lower layer fluid to escape beneath the shoaling wave (T_e), plunging breakers are governed by the time scale for the rear face to steepen to the vertical position (T_s) at the threshold of onshore overturning (Rayleigh–Taylor instability) and collapsing breakers are governed by the time scale for the separation bubble to form and reach the pycnocline leading to instability (T_b). These time scales were evaluated manually through flow visualizations. The predominance of a

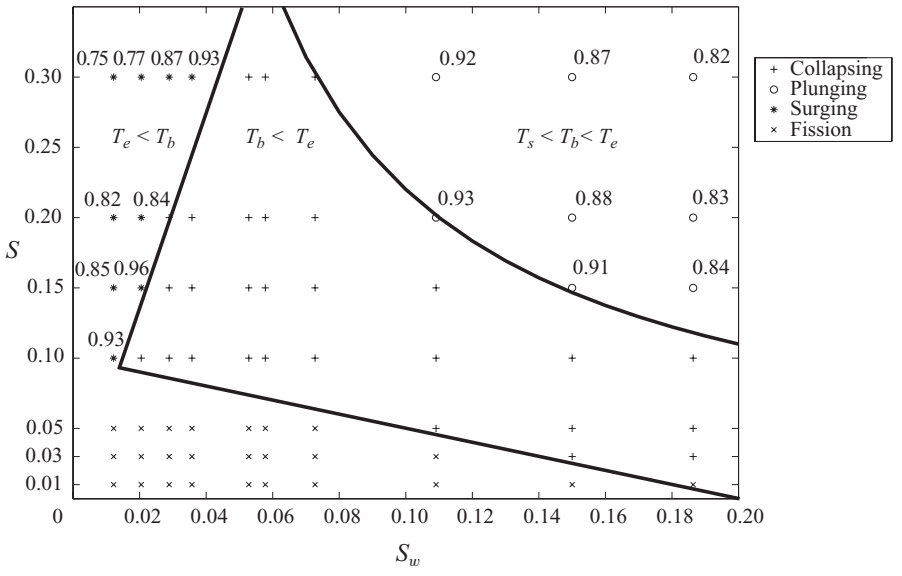

FIGURE 6. Different shoaling mechanism regimes according to the wave slope (S_w) and the boundary slope (S). Numbers beside stars and circles denote T_e/T_b and T_s/T_b, respectively.

particular breaking mechanism results from the relative time scales associated with their evolution. This is discussed below.

4.2. *Breaker types and their characteristics*

Four different degeneration mechanisms were observed in the simulations. These include three types of convective breakers (collapsing, plunging and surging) as well as fission. The mechanisms may be classified as a function of the wave and boundary slopes (figure 6). Spilling breakers, as observed by Boegman *et al.* (2005), were not found in the present simulations.

4.2.1. *Collapsing breakers*

Boundary-layer separation is the dominant mechanism leading to collapsing breakers (figure 7). The separated down-slope flow diverted by the separation bubble pushes the rear face of the wave down slope such that the wave collapses back upon itself as it shoals (figures 7*c* and 7*d*). This mechanism occurs before the lower layer fluid is discharged completely beneath the wave and prevents the rear face from steepening enough to be able to plunge forward. Collapsing breakers occurred for moderate wave slopes ($0.03 < S_w < 0.1$) over steep boundary slopes ($S > 0.1$) as well as steep waves ($S_w > 0.1$) over mild and moderate boundary slopes ($0.03 < S < 0.1$) (figure 6). The separation bubble eventually broke down into smaller vortices (figure 7*e*). This patch of vortices contained a mixing region which was pushed upslope by the inertia of the wave (figure 7*f*).

For steep waves over moderate and mild slopes, a positive tail started to form before wave breaking (figures 7*b* and 7*c*). The offshore directed upper layer horizontal velocity forced the crest of the positive tail down slope (figure 7*d*) favouring the collapsing breaker. Due to the shear increase at the crest of the positive tail, shear instabilities were possible and have been observed during breaking in the laboratory (Kao *et al.* 1985; Boegman *et al.* 2005; Hult, Troy & Koseff 2009). Local gradient Richardson numbers ($Ri = N^2/(\mathrm{d}u/\mathrm{d}z)^2$) less than 0.25 were simulated near the

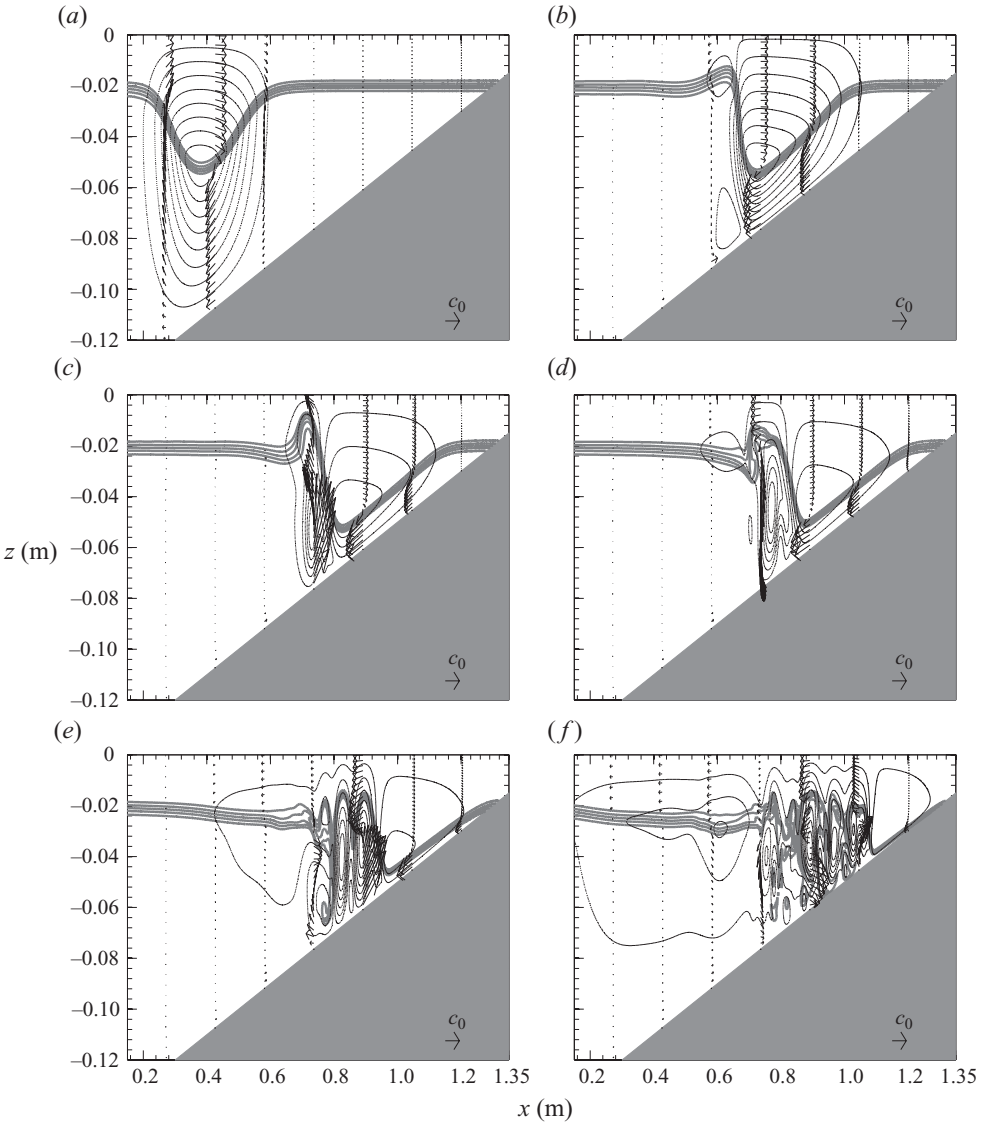

FIGURE 7. Successive images of a collapsing breaker (simulation 9). Solid lines are density contours and the dotted lines are streamlines. Instantaneous velocity field is shown by velocity vectors. For this simulation, linear phase speed is $c_0 = 0.081$ m s^{-1}. Figures (*a*) to (*f*) correspond to $tc_0/H = 14$, 16.7, 17.8, 18.4, 19.4 and 21.1, respectively.

pycnocline during breaking (figure 8; corresponding to figure 7*d*); however, shear instabilities were not evident during the simulations. The structure of the unstable region at the positive tail crest resembles the convective instability shown by Fringer & Street (2003; their figure 13). Here $Ri < 0.25$ is a necessary, but not sufficient, condition for shear instabilities, and their absence during the numerical simulations may result from (i) the growth periods being longer than the period of low Ri (Boegman *et al.* 2003; Troy & Koseff 2005; Fructus *et al.* 2009), (ii) the lack of infinitesimal perturbations within the numerical simulations from which instabilities will grow, and/or (iii) the possibility that shear instabilities are secondary three-dimensional

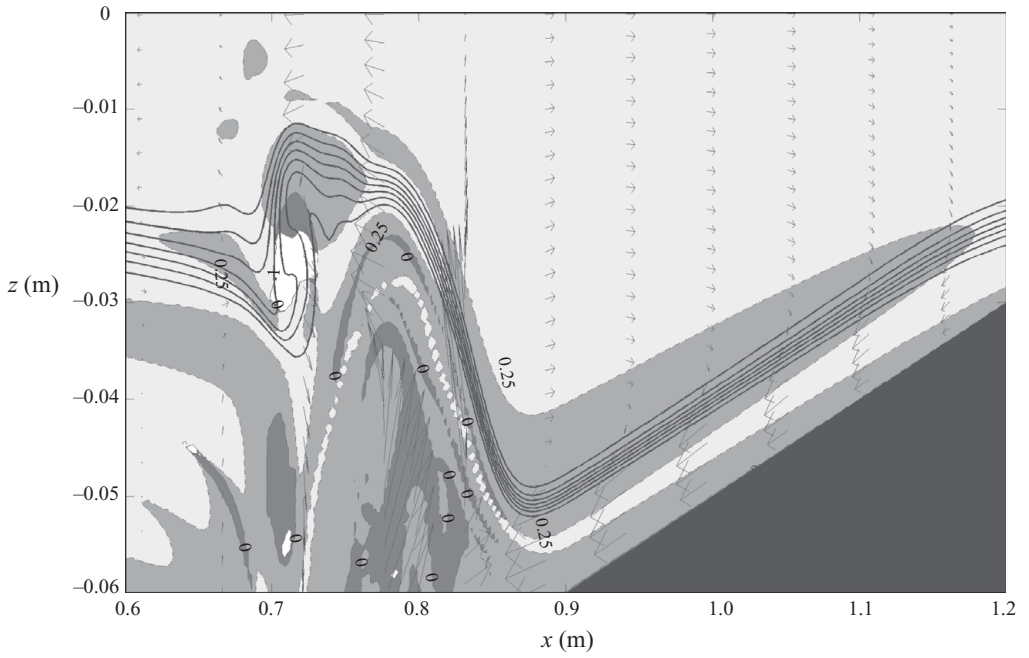

FIGURE 8. Spatial map of the instantaneous local gradient Richardson number near the positive tail formed during a collapsing breaker event (simulation 9). The grey shaded region shows $Ri < 0.25$ while the dark grey shaded region only shows $Ri < 0$. The contour lines show isopycnals. Note the occurrence of convective instability rather than Kelvin–Helmhotz instability at the crest of the positive tail at $(0.72, -0.015)$, where the pycnocline is being pushed offshore by the horizontal velocity field.

instabilities (Smyth & Peltier 1990; Fringer & Street 2003). The inability to model three-dimensional effects as the flow becomes turbulent is also evident in two-dimensional simulations of global instability (Carr *et al.* 2008).

4.2.2. *Plunging breakers*

The steepening of the rear face is the dominant process for plunging breakers (figure 9), where the rear face steepens (figures 9*b* and 9*c*) until it overturns in the onshore direction (figure 9*d*). Steep waves ($S_w > 0.1$) are more susceptible to overturning, especially over steep slopes ($S > 0.1$) where there is a sudden depth variation as the wave shoals. Hence, plunging breakers lie in the region of steep wave and boundary slopes (figure 6) where $S \geqslant 0.022/S_w$.

Despite the occurrence of boundary-layer separation beneath the wave, the rear face overturns forward before the flow induced by the separation bubble is able to modify the breaker type (T_s (figure 9*c*) $< T_b$ (figure 9*e*)). This forms the anvil structure of a Rayleigh–Taylor instability where the denser lower layer fluid accelerates into the less dense upper layer fluid (figure 9*e*). Mixed mode breakers were also simulated, where the boundary-layer separation dominates the breaking process just prior to plunging forward. These cases are considered as transitional breakers between collapsing and plunging which are shown by letters CP in table 1 ($T_b \approx T_s$). As with collapsing breakers, plunging breakers caused a significant amount of mixing during breaking. After the lower layer fluid was drawn out from beneath the wave, a mixing region comprised of vortices emanating from the plunging anvil was pushed upslope while

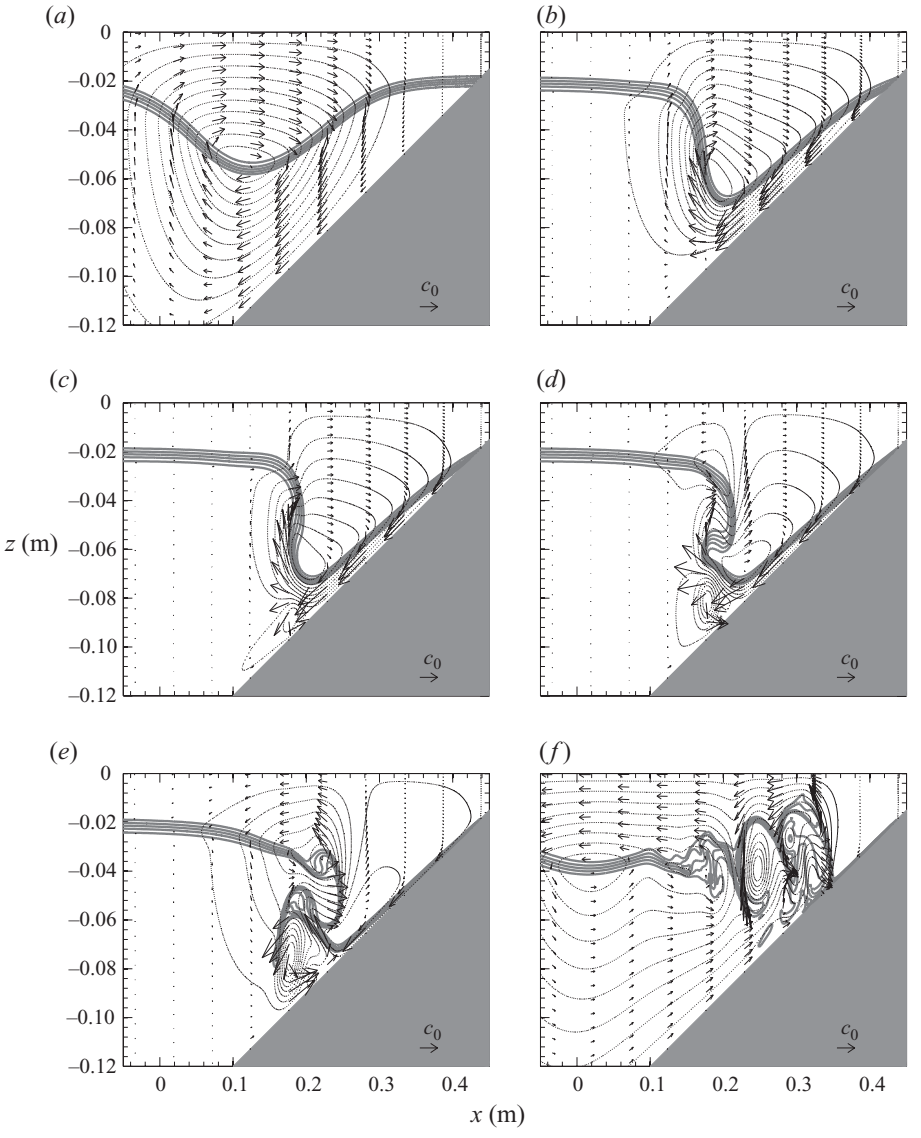

FIGURE 9. Same as figure 7 except for a plunging breaker (simulation 60). For this simulation, linear phase speed is $c_0 = 0.081$ m s^{-1}. Figures (a) to (f) correspond to $tc_0/H = 7.9, 8.7, 9, 9.2, 9.5$ and 10.8, respectively.

the leading face was reflected (figure 9f). A mixed region followed the reflected wave offshore as an intrusion within the pycnocline.

By analogy to surface breakers, plunging breakers have been conceptualized to occur when the horizontal velocity of the wave crest (u; here the horizontal velocity at the rear shoulder of the wave) exceeds a multiple of the linear deep water phase speed (c_0) (e.g. Peregrine 1983). Laboratory experiments (Sveen *et al.* 2002; Boegman & Ivey 2009) show plunging ISW breaking to occur when $u \sim 0.7c_0$. This is in good agreement with the present study where plunging occurs over $0.55 < u/c_0 < 0.9$ (figure 10). Over a given slope the more nonlinear (steeper) wave reaches a greater value of u/c_0 and a/H_s (H_s is local total depth) at the threshold of overturning. Conversely, the value

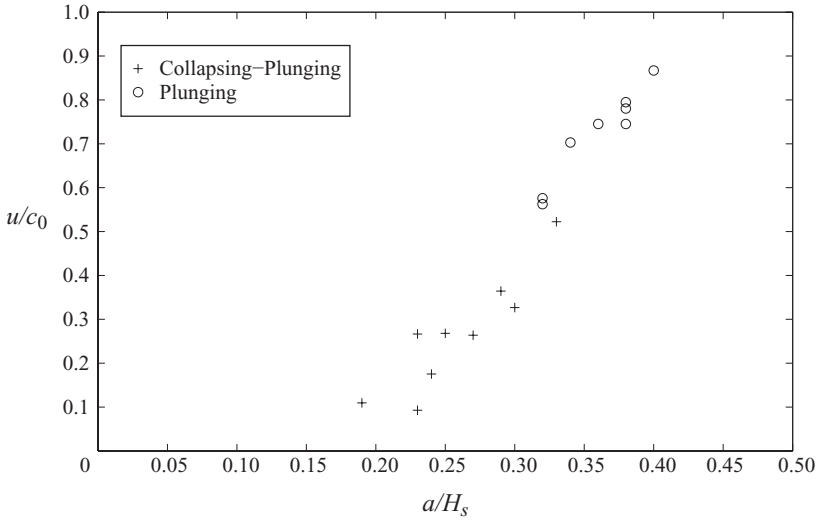

FIGURE 10. Horizontal velocity at the rear shoulder of the wave over linear phase speed (u/c_0) at the threshold of overturning versus the ratio of offshore wave amplitude over total depth at the threshold of overturning (H_s). The values of $u/c_0 > 0.55$ identify plunging breakers.

of u/c_0 at the threshold of breaking decreases for a given wave as the boundary slope increases.

Our results demonstrate that at the locations at which waves overturn the ratio of offshore wave amplitude (a) to local total water depth (H_s) is greater for steeper waves than for milder waves. Also, a given wave overturns in a relatively deeper water column as we increase the boundary slope. This is because over a gentler slope shoaling waves have more time to adjust to their changing environment. Therefore, a/H_s represents the contribution of steepening in the breaking process and for plunging breakers $a/H_s > 0.33$ (figure 10).

4.2.3. *Surging breakers*

For surging breakers, the wave trough reaches the sloping boundary before steepening and/or boundary-layer separation become significant (figure 11*d*; T_e). The pressure gradient and wave inertia cause the rear wave face to surge upslope while the leading face reflects from the boundary. This changes the flow direction to on-slope in the lower layer and off-slope in the upper layer (figure 11*e*). A separation bubble forms beneath the surging wave (figure 11*d*) and is pushed onshore by the flow to reach to the pycnocline (figure 11*e*; T_b), but occurs late in the shoaling process and at a negligible scale to influence the breaker type ($T_b > T_e$). Most of the wave energy is reflected with minimal mixing at the breaking location.

Surging breakers were observed when the wave slope was much smaller than the boundary slope. Since the wave slope was small, the deceleration beneath the rear face was weak and growth of a separation bubble was slow. Moreover, a mild-slope wave takes longer to steepen effectively and overturn. Given these constraints, surging breakers were found to occur where $S \geqslant 7S_w$ (figure 6). In some simulations mixed mode collapsing and surging breakers would occur and the separation bubble would detach from the collapsing rear face, surging up the slope; in this situation, $T_b \approx T_e$ (CS in table 1). However, the dominant process is boundary-layer separation, thus they have been classified as collapsing breakers in figure 6.

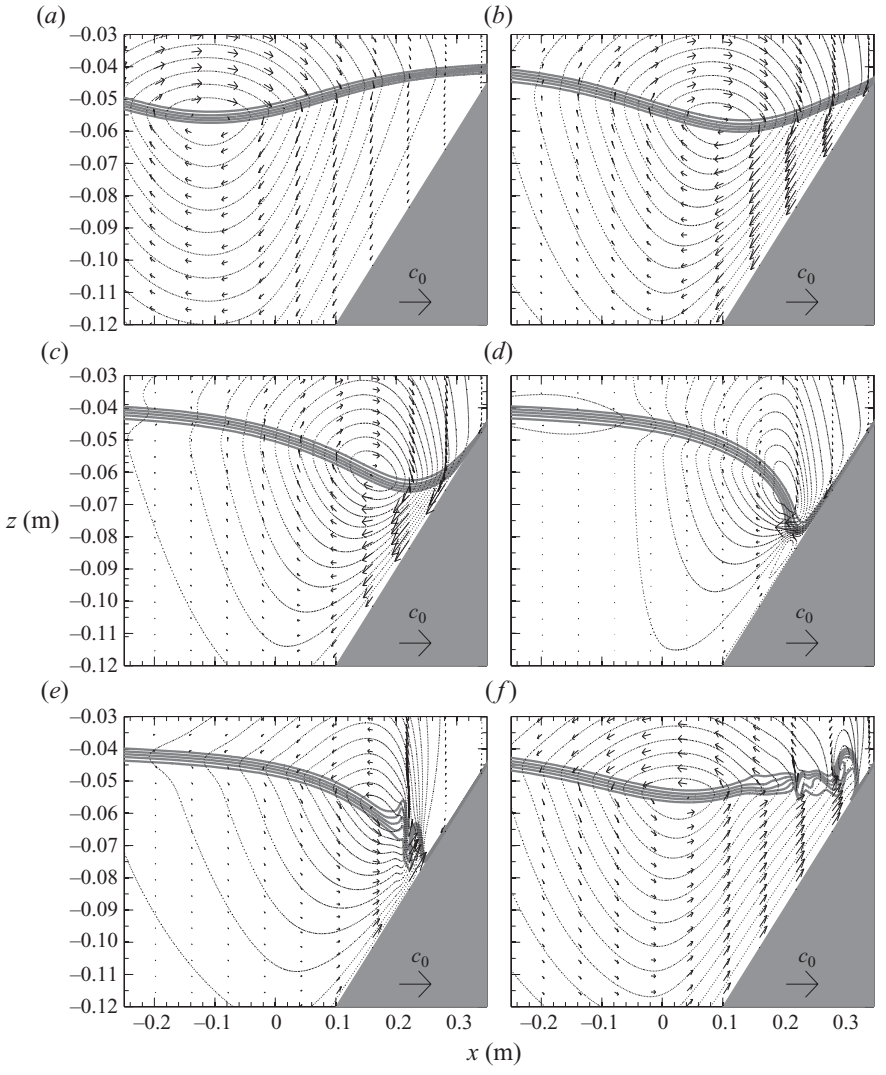

FIGURE 11. Same as figure 7 except for a surging breaker (simulation 55). For this simulation, linear phase speed is $c_0 = 0.105$ m s^{-1}. Figures (*a*) to (*f*) correspond to $tc_0/H = 8.4, 9.8, 10.5, 11.2, 11.9$ and 13.3, respectively.

The surging process plays an important role after breaking, in all breaker types, by pushing the mixed region onshore, which in turn can transport suspended sediments upslope (Boegman & Ivey 2009). After breaking occurs, turbulent boluses (cores of mixed fluid; Helfrich 1992) form close to the surging region (figure 12) following the initial separation bubble. The down-slope flow of the lower layer fluid behind a moving bolus interacts with the upslope surge leading to the generation of the next bolus. Following Helfrich (1992) we found that the number of boluses decreases with λ/L_i (figure 13); however, Helfrich observed more boluses for a given λ/L_i. The boluses propagate upslope until they ultimately degenerate through three-dimensional instability (Venayagamoorthy & Fringer 2007).

Following Helfrich (1992), we plot D_b/a versus λ/L_i (figure 14). Here D_b is the thickness of the first bolus which is also the thickness of the separation vortex formed

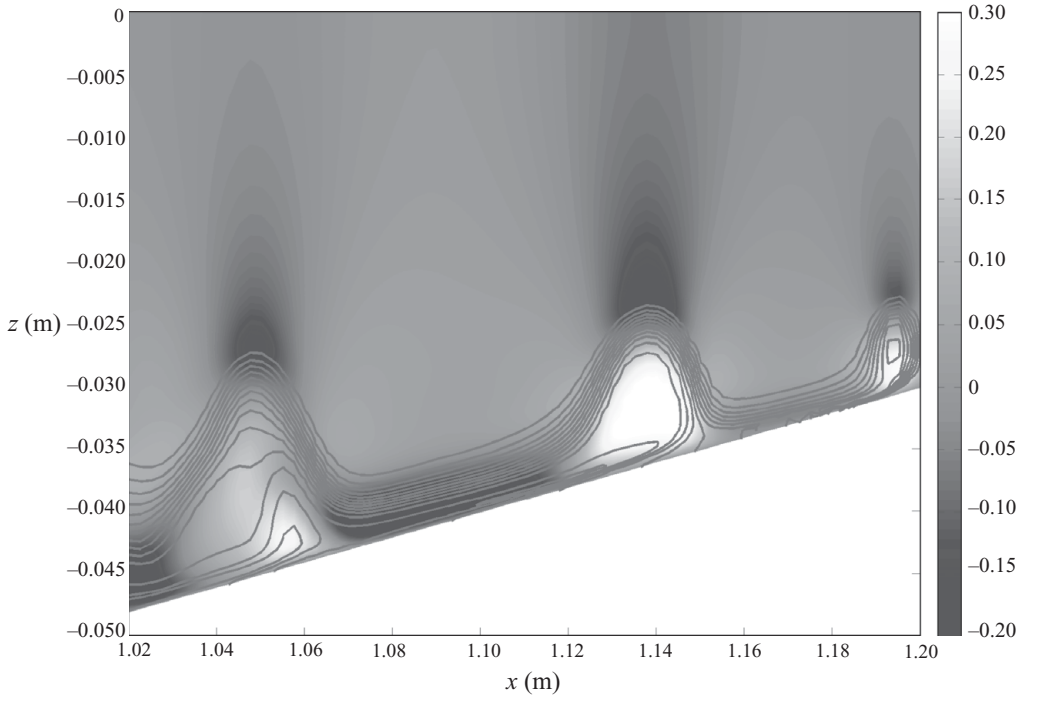

FIGURE 12. Turbulent boluses generated by a collapsing breaker moving onshore due to surging effect (simulation 3). Shaded areas represent non-dimensional horizontal velocity field (u/c_0) and solid lines are isopycnals.

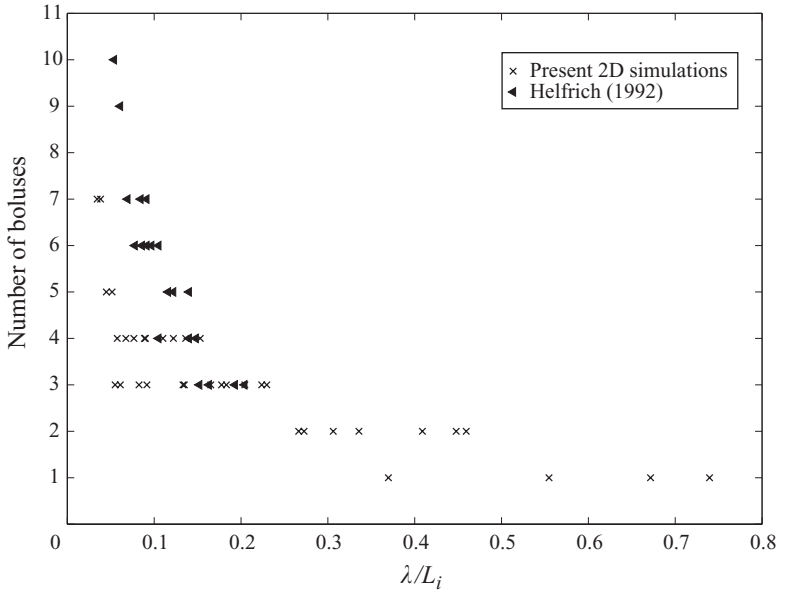

FIGURE 13. Number of boluses versus (λ/L_i) following Helfrich (1992). 2D, two-dimensional.

via boundary-layer separation. Our data are consistent with Helfrich's results showing $D_b/a = 1.75 \pm 0.25$ over $0 < \lambda/L_i < 0.25$. However, we find that D_b/a decreases with increasing λ/L_i over the wider parameter range considered in this study. Helfrich

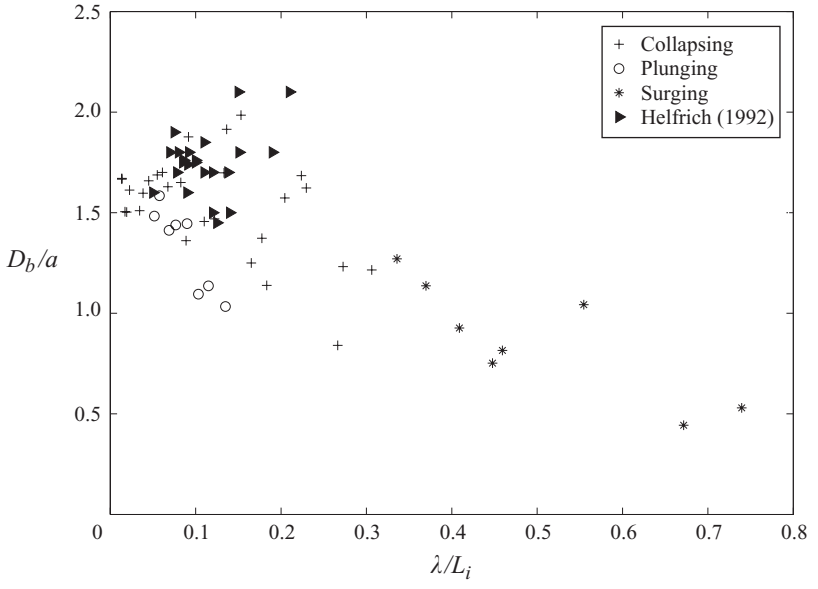

FIGURE 14. Separated region thickness (first bolus according to Helfrich 1992) over offshore wave amplitude (D_b/a) versus (λ/L_i). Here λ is the horizontal scale of the offshore wavelength according to the KdV equation.

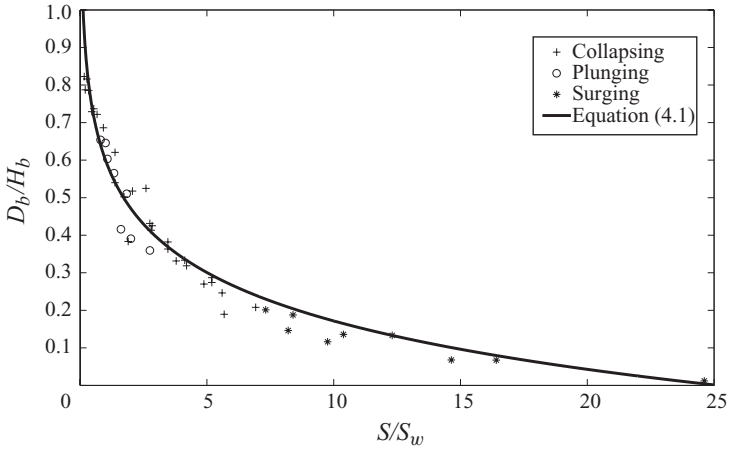

FIGURE 15. Separated region thickness over total depth (D_b/H_b) at the breaking point as a function of the boundary slope to wave slope ratio (S/S_w).

(1992) only considered a narrow range of mild slopes ($0.034 < S < 0.067$), and so the difference in figure 14 is to be expected. This is because a greater value of λ/L_i in general corresponds to a milder wave slope relative to the boundary slope leading to more effective surging where the flow separation is relatively weak.

To differentiate surging from collapsing breakers, D_b was compared to the total depth at the location where separation vortex has reached the pycnocline (H_b). Pure surging breakers lie in the region $D_b < 0.2H_b$ (figure 15). Here D_b/H_b can be modelled

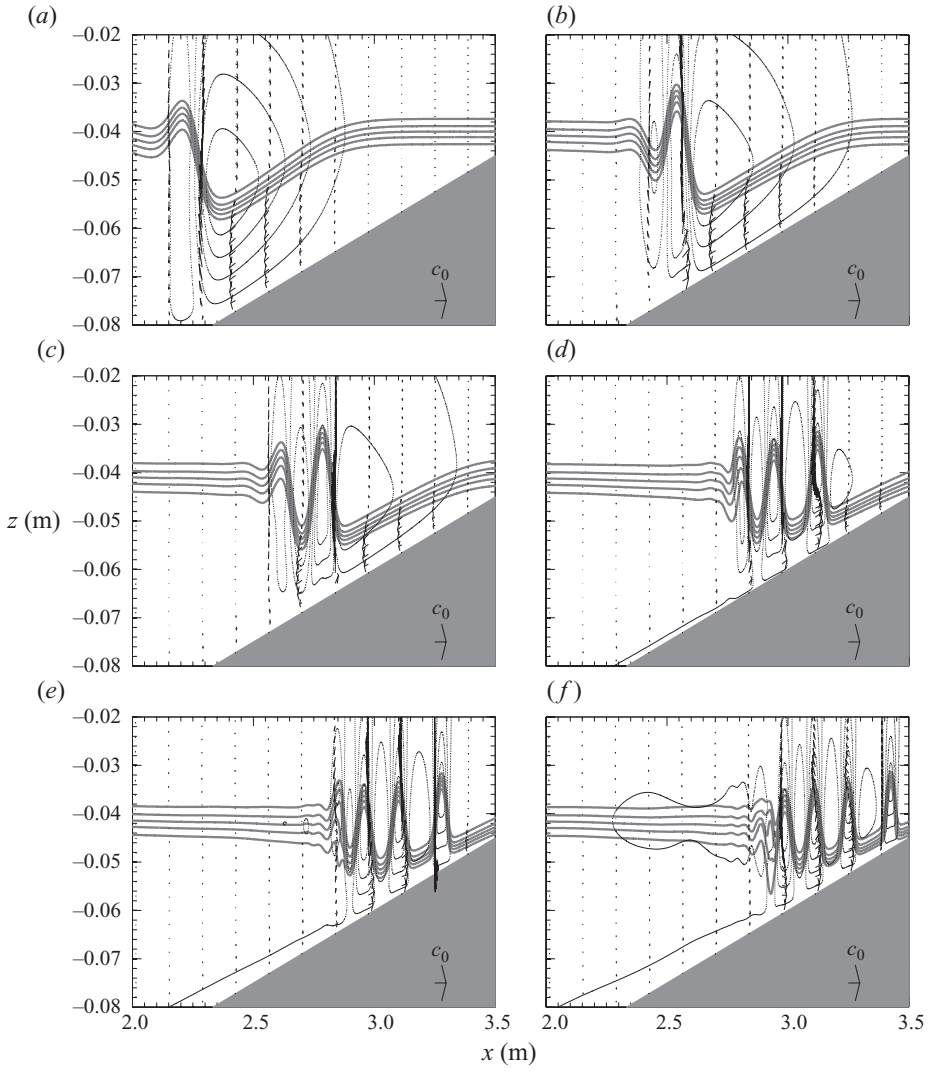

FIGURE 16. Same as figure 7 except for a fissioning wave (simulation 25). For this simulation, linear phase speed is $c_0 = 0.105$ m s^{-1}. Figures (a) to (f) correspond to $tc_0/H = 30.4, 33.6, 36.1, 39.9, 41.8$ and 43.7, respectively.

as a function of S and S_w, which are external to the breaking process

$$\frac{D_b}{H_b} = -0.186 \ln \frac{S}{S_w} + 0.6 \tag{4.1}$$

and may be interpreted as the thickness of the initial sediment re-suspending core that moves onshore (e.g. Boegman & Ivey 2009).

4.2.4. *Fission*

Over gentle slopes an incident wave of depression will degenerate through fission, forming a packet of waves of elevation as it passes through the turning point where $h_1 = h_2$ (figure 16). This shoaling process occurs very gradually over longer time scales

than the wave-breaking processes described above. The slow steepening of the rear face of the wave occurs because the water depth is changing slowly and hence, in the context of the KdV equation, the nonlinear and dispersive parameters are varying slowly. Thus, the steepening is insufficient to cause overturning. The adverse pressure gradient beneath the rear face leading to the generation of a separation bubble also grows gradually; thus collapsing does not rapidly occur. In figure 6 the region where $S < -0.5S_w + 0.1$ corresponds to fission.

The fission process can be understood by looking at the variation of the quadratic nonlinearity coefficient α along the slope. Over a uniform slope α varies gradually before approaching zero at the turning point and rapidly increasing thereafter (Zhao *et al.* 2003; their figure 4). The dispersion coefficient in the KdV equation decreases gradually as well. These variations (together with variations of higher-order nonlinear and dispersive parameters) result in the transformation of the incident ISW of depression to a packet of waves of elevation.

This transformation occurs as the positive tail forms behind the wave and locally moves the interface upward (figure 16*a*). An offshore horizontal flow in the upper layer and an onshore horizontal flow in the lower layer is generated (figure 16*a* and §4.1). These dynamics transform the wave polarity as it moves onshore (figure 16*b*). The wave of elevation is formed in a region of positive polarity (positive nonlinear coefficient in the KdV equation) and it is followed by a step-like structure, which again transforms to another ISW of elevation (figure 16*c*). This process continues and a packet of waves of elevation moves onshore along the tilted front face of the initial wave. Although the positive tail also forms over steep slopes, other mechanisms (boundary-layer separation or overturning) occur over shorter time scales, leading to wave breaking before fission into a packet of waves of elevation. The fission process did not give rise to significant turbulent diapycnal mixing or reflection. Most of the wave energy was lost to viscous damping (dissipation). However, our two-dimensional simulations do not necessarily correctly partition irreversible energy losses to diapycnal mixing and dissipation (Lamb *et al.* 2005). The fission mechanism associated with emerging ISWs is distinct from that associated with turbulent boluses, where wave inertia pushes a mixed breaking region shoreward. ISWs of elevation with trapped cores, similar to figure 12, have been observed in the ocean (e.g. Klymak & Moum 2003).

Shroyer *et al.* (2009) investigated the fission process by calculating the vorticity field and variations of α as ISWs shoal upon the New Jersey coast. They showed that a sign change of α correlates well with the vorticity sign reversal at the trough of the ISW, which implies that the fission process is occurring. We have simulated fission processes occurring before and after the turning point location. The discrepancy is likely due to the uncertainty in identifying the location of the turning point in field observations and the necessity of Shroyer *et al.* (2009) to adjust the vorticity reversal point to account for background shear. The fission process has also been shown in theoretical and numerical studies to occur from a gradual change in the sign of the quadratic nonlinearity coefficient in the KdV equation (e.g. Talipova, Pelinovskii & Grimshaw 1997; Grimshaw *et al.* 1998) with fission occurring when the time scale of nonlinearity change is longer than the waveperiod ($T = L_w/c$). To analyse the fission process quantitatively, we compared L_w and L_i (figure 1). For smaller values of L_w/L_i, fission is more likely because for a given wave, by decreasing the boundary slope the wave has more time to adjust to the changing water depth, in agreement with the results of others (e.g. Grimshaw *et al.* 1998). Conversely, in some of our simulations over gentle slopes, we observed that the fission process occurs for waves with greater

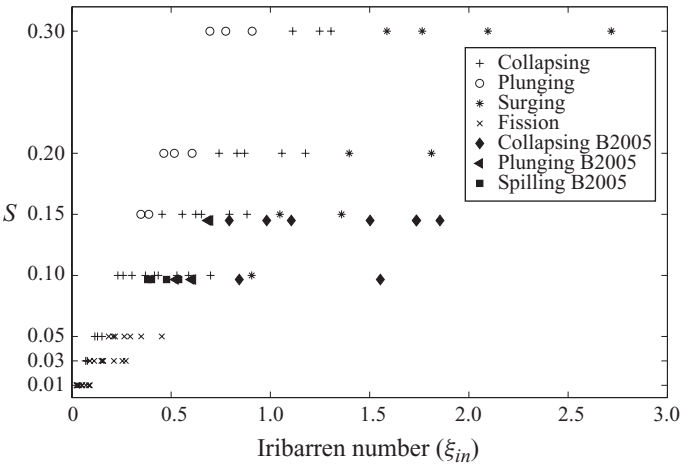

FIGURE 17. Type of breaking as a function of internal Iribarren number. Experimental results of Boegman *et al.* (2005) are distinguished by B2005.

L_w and by decreasing L_w the shoaling process tends towards a collapsing breaker (simulations 22–31 and 32–41; table 1). This means that in some of our simulations, for a greater value of L_w/L_i, fission is more probable (figure 5), which is in contrast with previous studies.

The differences between our results and those of Talipova *et al.* (1997) and Grimshaw *et al.* (1998) may be because their analytical studies do not capture as much physics as the present fully nonlinear simulations. In the analytical study by Grimshaw *et al.* (1998), only the quadratic nonlinearity coefficient was varied and all other coefficients were held constant. Another parameter that contributes to fission is the initial nonlinearity of the wave which was not considered by Grimshaw *et al.* (1998). There is a stronger adverse pressure gradient beneath a more nonlinear wave which can grow quickly enough to cause collapsing instead of fission, no matter how small L_w/L_i is.

5. Discussion

5.1. *Breaking criteria*

Our simulations show that for moderately steep boundary slopes ($S \geqslant 0.1$), the breaking mechanism trends from surging to collapsing then plunging with increasing wave slope. On the other hand, if the slope is mild ($S \leqslant 0.05$) the shoaling mechanism trends from fission to collapsing with increasing wave slope (figure 6). These results suggest that the breaking mechanism may be modelled in a deterministic manner.

Boegman *et al.* (2005) proposed that ISW breaking could be modelled according to an internal form of the Iribarren number (1.1), which is universally applied to model surface breaker types. The results from the present study and the laboratory results given in Boegman *et al.* (2005) are directly compared using ξ_{in} to model the ISW breaking mechanism (figure 17). Their data cover a narrow range of boundary slopes (0.1–0.15) and show the same trend from plunging to collapsing with increase of the Iribarren number. However, for a given S they observed plunging breakers for larger ξ_{in} (smaller S_w) compared to our data. This is likely due to the shoaling

ISWs in Boegman *et al.* (2005) being carried on a background basin-scale seiche and nonlinear surge oscillations from which the ISWs evolved during the course of the experiments. The background flow increases upper and lower layer velocities above and beneath the wave respectively favouring the forward overturning (Boegman *et al.* 2005; their figures 8 and 9).

Mixed mode breaking, with a contribution from shear instabilities was observed in the experiments by Boegman *et al.* (2005), but did not occur in the present simulations. Boegman *et al.* (2005) observed shear instabilities where shoaling ISWs of elevation had passed through the turning point and the wave crests approached the surface boundary of their flume. The shear at the wave crests was increased due to the no-slip surface boundary necessitating larger mid-layer velocities in order to maintain conservation of volume. The wave crests were sheared off as they propagated upslope. These were erroneously labelled spilling breakers by Boegman *et al.* (2005). Shear instabilities similar to their spilling breakers were observed at the crests of boluses in some of our simulations; however, our simulations did not employ a no-slip surface boundary.

Boegman *et al.* (2005) also observed mixed mode breaking with shear instabilities when the space-time-varying background flow field induced by the baroclinic seiche was strong. Our simulations did not include seiche dynamics, and so this breaking mechanism was not expected. The space-time-varying background flow field and along-slope advection of the pycnocline-slope interface would greatly influence the breaker type for a particular Iribarren number relative to the quiescent background flow considered in the present study. More laboratory experiments are required to validate the numerical results presented herein.

Our results differ from those of Fringer & Street (2003), who found the breaking mechanism (shear/convective) to depend on the wave steepness and pycnocline thickness. We attribute the difference to the presence of a sloping bottom boundary in the present study; the breaker type depends on the influence of both the wave and boundary parameters in regulating convection, flow separation and fission processes (S versus S_w domain; figure 6). Sensitivity to d_{pyc} was not part of the present study. However, doubling d_{pyc} in simulations 1-10 did not change the breaker type. This is not unexpected; our modelled wave-slope collision breakers are convective, whereas those away from slopes are susceptible to shear instability and hence more sensitive to interfacial thickness (Fringer & Street 2003).

5.2. *Breaking location*

The breaking location is a localized region where dissipation, mixing and resuspension are elevated relative to background values. It is of physical and biogeochemical importance to develop parameterizations to predict the breaker location, which will aid in determining locations for field measurements and high-resolution computational model grids.

For surface breakers the ratio of the wave amplitude to the local breaking depth proves to be a deterministic parameter in modelling the breaking location (Dean & Dalrymple 1991). Similarly, Helfrich (1992) found that for internal waves, the ratio of the wave amplitude to the local undisturbed lower layer depth (h_{2b}) characterizes the breaking location. The tendency for a/h_{2b} to increase as λ/L_i decreases was also found to be valid for steeper slopes (figure 18), supporting the observation that larger waves tend to propagate into slightly shallower water (relative to their initial amplitude) before breaking (Helfrich 1992). The results from the present study agree

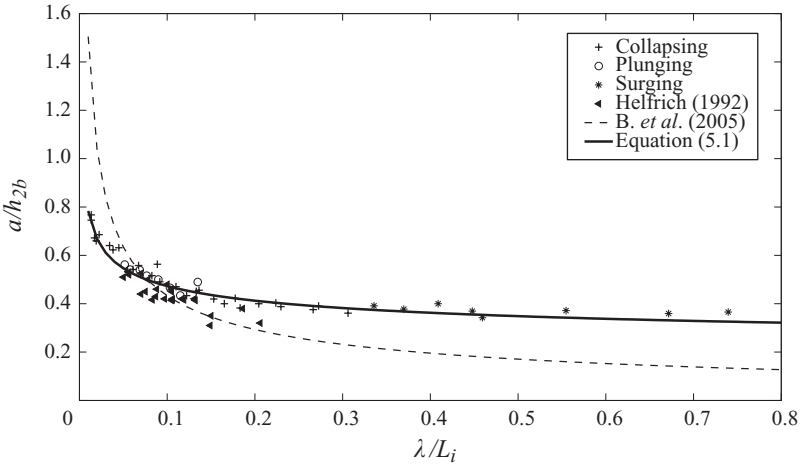

FIGURE 18. A breaking location criterion: ratio of initial wave amplitude over undisturbed lower layer thickness at breaking location (a/h_{2b}) versus λ/L_i, where λ is a measure of the offshore wave horizontal length according to the KdV equation. The dashed line is given by the equation proposed by Boegman *et al.* (2005) and the solid line is given by our proposed equation (5.1).

qualitatively with the results given by Helfrich (1992), and we propose

$$\frac{a}{h_{2b}} = \frac{0.14}{(\lambda/L_i)^{0.28}} + 0.13 \tag{5.1}$$

to predict the breaking location of ISWs over sloping boundaries. Figure 18 shows that the more intense breaking events (collapsing and plunging) occur where $a/h_{2b} > 0.4$, consistent with Helfrich (1992). This is also consistent with field observations of Moum *et al.* (2003), where they detected non-breaking ISWs with $a \sim 20$ m shoaling over Oregon's shelf where $h_{2b} \sim 86$ m ($a/h_{2b} = 0.23 < 0.4$). As is expected from the KdV theory, the location of the polarity change at the turning point also plays an important role in determining the breaker type relative to the breaking location. Energetic wave-breaking events (collapsing and plunging) tend to occur mostly offshore of the turning point, which is in agreement with laboratory observations (Boegman *et al.* 2005). Large S will result in small L_i, leading to rapid plunging or collapsing prior to the wave reaching the turning point. Fission occurs via the gradual polarity change through the turning point which is allowed to proceed for small S and tends to occur mostly onshore of the turning point. For a given slope the more nonlinear wave (steeper wave) tends to break further offshore of the turning point (figure 19). For the case of fission, the breaking point is defined as the location where the first wave of elevation emerges.

5.3. *Energy reflection*

Another important parameter in studying the breaking of ISWs upon sloping topography is the reflection coefficient ($R = E_r/E_i$), where E_i and E_r are incident and reflected wave energies, respectively. The proportion of incident wave energy lost to mixing and dissipation is given by $1 - R$. This is important to close the energy budget and determine the fate of observed shoreward-propagating internal waves.

Helfrich (1992) showed that R increases with λ/L_i. Michallet & Ivey (1999) modelled R in terms of the ratio of the wavelength (L_w) to the slope horizontal length (L_s).

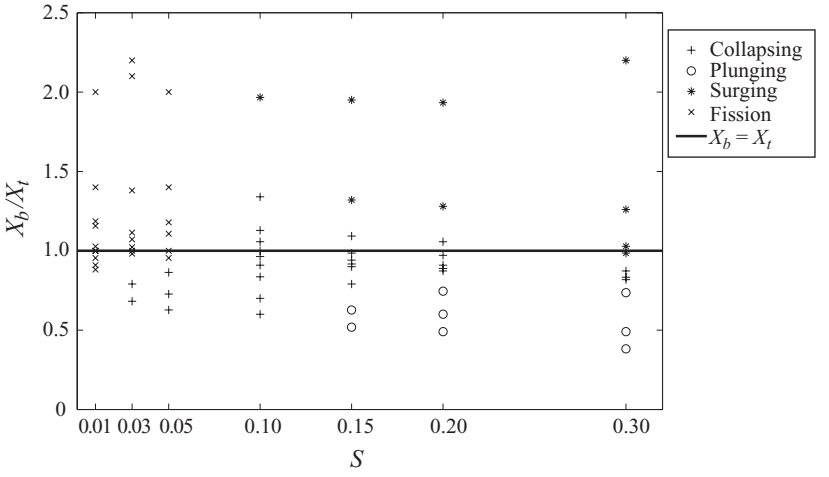

FIGURE 19. The ratio of the breaking point location (X_b) over turning point location (X_t) versus boundary slope. Here X_b and X_t denote horizontal distances from the toe of the slope to the breaking and turning points, respectively. The greater value of X_b/X_t for each slope corresponds to the less nonlinear wave (smaller wave front slope).

Boegman *et al.* (2005) generalized these results to the field scale by modelling R in terms of the internal Iribarren number. Bourgault & Kelley (2007) subsequently addressed the potential impacts of sidewall friction in contaminating the laboratory data of Helfrich (1992) and Michallet & Ivey (1999).

Comparisons between laboratory observations and numerical studies show R to be well modelled in two-dimensional simulations that do not fully resolve the three-dimensional turbulence occurring during wave breaking (Bourgault & Kelley 2007; Lamb & Nguyen 2009). We argue that this is because the reflected energy is determined during the initial two-dimensional wave/slope interaction occurring at a large scale (Bourgault & Kelley 2007). The secondary three-dimensional instability (Fringer & Street 2003) that leads to turbulent dissipation ε and irreversible buoyancy flux b is not modelled. Two-dimensional simulations overestimate b and underestimate ε relative to the three-dimensional case (Fringer & Street 2003; Lamb *et al.* 2005). Given that $R = E_r/E_i = (E_i - b - \varepsilon)/E_i$, these effects offset and the total irreversible energy loss $(b + \varepsilon)$ is captured (hence R is correct), but the mixing efficiency $R_f = b/(b + \varepsilon)$ will be incorrect.

We follow the methods of Lamb (2007; (31) therein) and directly calculate the incident and reflected wave energy fluxes through a plane at the toe of the slope. The domain is sufficiently long that this prevents contamination of the energetics calculations from secondary breaking events (Michallet & Ivey 1999). The internal Iribarren number, which incorporates boundary and wave slope in a fractional formula (see (1.1)), was used to model the reflection coefficient (figure 20). There is no reflected wave associated with the fission mechanism and $R \to 0$ as $S \to 0$ (all incident energy is eventually lost to viscous dissipation with minimal mixing). As expected, most of the wave energy is reflected off the slope in case of surging breakers.

The results agree with the parameterization proposed by Bourgault & Kelley (2007), with the exception of collapsing breakers as discussed above. There is qualitative agreement between our results and the data from Michallet & Ivey (1999), except their data have systematically lower R values. This may be due to viscous damping

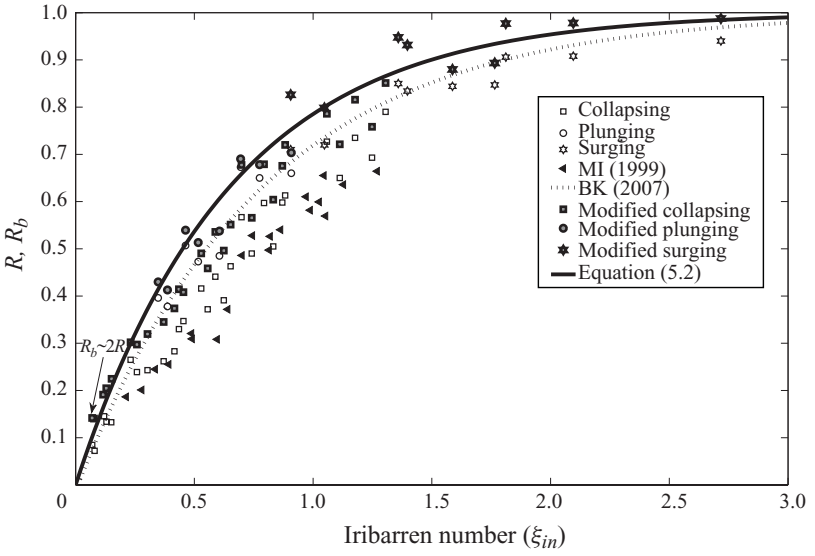

FIGURE 20. Reflection coefficient (R) versus internal Irribarren number (ξ_{in}). Filled symbols show the modified reflection coefficient values at breaking point (R_b). The dotted line represents the equation $R = 1 - \exp(-\xi_{in}/0.78)$ proposed by Bourgault & Kelley (2007) and the solid curve is our proposed equation (5.2) for R_b.

along the side walls of their flume causing energy loss and reduced R (Bourgault & Kelley 2007).

In all previous studies and so far in this study, R was measured at the beginning of the slope, meaning that viscous losses occurring prior to wave breaking for the incident wave and after wave breaking for the reflected wave were neglected. This will cause R to systematically decrease as the bottom slope decreases. Helfrich (1992) performed his experiments upon mild slopes ($0.03 < S < 0.067$) which most probably caused his R values to be well below those of other studies (Bourgault & Kelley 2007; their figure 6). This indeed occurs for collapsing breakers in our simulations (figure 20).

In a more comprehensive approach we calculated viscous losses during incident wave movement from the beginning of the slope to the breaking point (ΔE_i) as well as during reflected wave movement from the breaking point to the toe of the slope (ΔE_r). The dissipation rate was calculated following Lamb & Nguyen (2009; (12) therein). We found that an ISW can lose up to 30 % of its energy via viscous damping before breaking and up to 25 % of the reflected wave energy could be lost while travelling towards the toe of the slope. On the basis of the revised calculations we introduce a breaking point reflection coefficient $R_b = (E_r + \Delta E_r)/(E_i - \Delta E_i)$ which represents the actual portion of the wave energy lost to mixing and dissipation via breaking ($1 - R_b$). Figure 20, where R and R_b are plotted as functions of the internal Iribarren number, shows that R_b can be up to $2R$, particularly for small Iribarren numbers for which the slope is small and the slope length is long. We propose a function (5.2) with $R^2 = 0.94$ which is a modified version of the equation proposed by Bourgault & Kelley (2007) to parameterize R_b versus ξ_{in}

$$R_b = 1 - \mathrm{e}^{-\xi_{in}/0.65}. \tag{5.2}$$

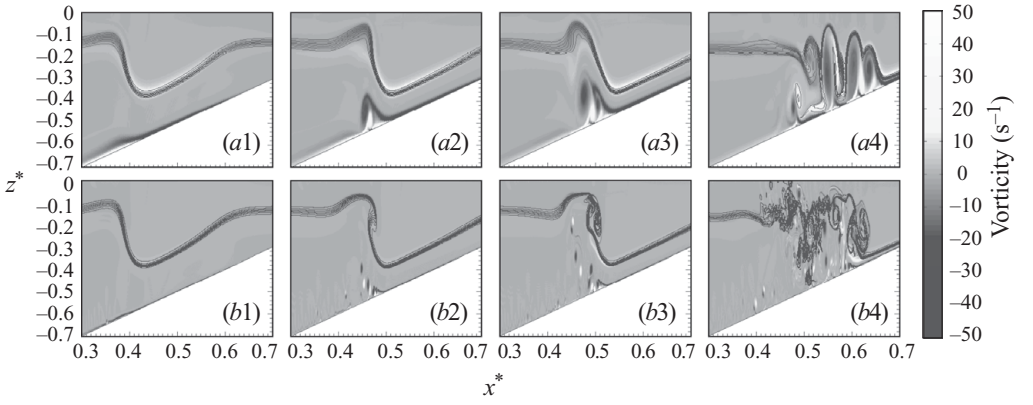

FIGURE 21. Successive images of vorticity (shading) overlain with isopycnals (solid lines). ($a1$–$a4$) Results from simulation 9 ($Re_w = 2.67 \times 10^3$) and ($b1$–$b4$) results from simulation 9b ($Re_w = 8.43 \times 10^4$) which is performed using 10 times larger scales compared to simulation 9. Vortex shedding and global instability are obvious in the high-Reynolds-number case. Horizontal coordinate is scaled by horizontal length of the slope ($x^* = x/L_s$) while vertical coordinate is scaled by total depth ($z^* = z/H$).

5.4. *Boundary-layer separation and effects of Reynolds number change*

Boundary-layer separation is the controlling process leading to collapsing ISW breakers; thus it is instructive to study this phenomenon in more detail. Carr & Davies (2006) found that over a flat bottom, the adverse pressure gradient beneath the wave strengthens as the wave amplitude increases, resulting in a faster growing separation bubble beneath a more nonlinear ISW. Diamesis & Redekopp (2006) found that the Reynolds number $Re = Hc_0/\nu$ provides a limiting criterion for the evolution of separated boundary layer into a global instability where the shed vortices are ejected away from the bed. Stastna & Lamb (2008) showed that for ISWs of elevation there should be a background current opposite to the wave propagation direction for global instability to occur and associated coherent structures can re-suspend bed sediments up to 25 % of the water column depth.

In this study, we investigated the relationship between wave slope and boundary-layer separation for closed slopes at laboratory scale. Here, we extend our results to include Reynolds number effects. To include the contribution of wave amplitude, Boegman & Ivey (2009) introduced a wave Reynolds number $Re_w = ac_0/\nu$ where typically, $Re_w \sim 10^3$ in the laboratory, $Re_w \sim 10^6$ in lakes and $Re_w \sim 10^7$ in oceans. We investigated the effects of larger Re_w by increasing the length scales in Re_w in simulation 9 by a factor of 10 such that Re_w increased from 2.67×10^3 to 8.43×10^4 (simulation 9b). The characteristics of the boundary-layer separation are shown with the vorticity fields (figure 21). Horizontal and vertical grid numbers were made four times larger for this simulation (600 vertical grid lines). For the large Re_w simulation, boundary layer instability occurs with multiple shed vortices that are smaller relative to the wave amplitude and have slower growth rates relative to the small Re_w case. This results from the boundary layer being thinner relative to the total depth for the large Re_w case (hence smaller shed vortices). The small vortex diameter and slow growth minimizes the influence of the flow separation on wave breaking with the result that steepening of the rear face of the wave is unencumbered and able to initiate plunging (figure 21.$b2$). Conversely, for small Re_w, the large and rapidly

growing bubble causes the wave to collapse prior to possible plunging. Clearly, the Reynolds number influences the breaking mechanism.

The large Re_w case is similar to the global instability phenomenon typically observed beneath large ISWs progressing over a flat bottom (e.g. Diamesis & Redekopp 2006). When the cluster of detached vortices reaches the rear face of the wave it becomes unstable (figure 21.*b*3) and a local portion of the wave collapses. The cluster of small vortices thus acts in a manner similar to the large vortices occurring at low Re_w. Interestingly, shed vortices reach the wave front at the same location along the slope and so the breaking location does not change with Re_w. Increasing Re_w causes an increase in R from 0.23 to 0.37. Lamb & Nguyen (2009) found an increase in R with Reynolds number for a wider range of Iribarren numbers. It has been argued above that R is determined by the primary two-dimensional instability and distance the wave travels along the slope prior to breaking. The increase of R with Re_w is likely due to reduced viscous dissipation, relative to the incident wave energy, associated with relatively smaller boundary-layer separation bubble in the large Re_w case.

5.5. *Implications for field-scale modelling*

Having modelled the instability processes leading to ISW breaking over sloping boundaries at laboratory scales ($Re_w \sim 10^3$), we discuss the implications of our results on large-scale modelling ($Re_w \sim 10^6$–10^7). As described above, it is necessary to resolve the bottom boundary layer in order to capture boundary-layer instability in simulating ISW breaking. This demands a fine grid resolution close to the bottom boundary. For example, in simulation 9 the non-dimensional boundary-layer thickness (δ/H) under the offshore wave trough was 0.028 and was resolved with six vertical grid lines. By increasing Re_w (increasing length scales in simulation 9b), the non-dimensional boundary-layer thickness became 0.006 and was resolved with five vertical grid lines. A benefit of σ-coordinates is that vertical resolution is finer in the shallower region where breaking occurs. For the high Reynolds simulation there were 44 vertical and 12 horizontal grid lines inside the smallest vortex. Similar results were obtained when the resolution was doubled. The resolution required to resolve the near-bed velocity gradients at $Re_w \sim 10^6$–10^7 at field scale is thus computationally prohibitive. To model a ~3 m amplitude wave in a 15 m water column (i.e. simulation 9 at 100 times larger physical scale with $Re_w = 2.67 \times 10^6$), we would need 2400 grid lines in the vertical direction (16 times more compared to simulation 9). This simulation would require ~300 GB memory to capture the shoaling process until the wave breaks.

Lorke (2007) presented horizontal velocity profiles at the bottom boundary of Upper Lake Constance at the depth of 11 m (his figure 8) where the boundary-layer thickness is ~0.11 m ($\delta/H = 0.01$). This value is close to the 0.1–0.15 m boundary-layer thickness observed in central Lake Erie (Boegman, unpublished data). Many field-scale numerical simulations of internal wave shoaling do not have sufficient vertical grid resolution to resolve these bottom boundary layers. For example, $\Delta z = 0.53$ m (Lamb 2002), $\Delta z = 3.3$ m (Legg & Adcroft 2003), $\Delta z = 0.5$ m (Bourgault & Kelley 2003) and $\Delta z = 6$ m (Vlasenko & Staschuk 2007). These values are larger than the boundary-layer thickness and thus these simulations (some of which did not use a no-slip bottom boundary condition and hence were also missing some essential physics) were not capable of capturing the flow separation processes central to regulation of the breaking mechanism.

The two-dimensional field-scale simulations by Vlasenko & Hutter (2002) are similar in configuration to the present study, but at larger Re_w. They used a no-slip bottom boundary condition with a vertical grid resolution of 0.5 m in modelling shoaling of a large ISW with 84 m amplitude where the total depth was 250 m. They simulated

plunging breakers and observed the anvil structure associated with a Rayleigh–Taylor instability (their figure 6); however, flow separation was not simulated to occur as is expected in a plunging breaker. This is likely due to their coarse grid resolution which was unable to resolve boundary-layer separation. As an alternative, vertically varying resolution has been effectively applied to resolve bottom boundary layer beneath ISWs (Diamesis & Redekopp 2006; Stastna & Lamb 2008) particularly for $Re_w \sim 10^4$.

Background currents and topographic roughness effects have not been considered in this study. These will occur in the field and will modify the breaking processes relative to our findings. Currents and roughness can readily be included in high-resolution σ-coordinate models (Stastna & Lamb 2008) and future work in this area is recommended.

6. Conclusions

We have extended the work of previous studies simulating shoaling processes of internal solitary waves upon sloping topography. Four breaking processes occurred: collapsing, plunging, surging and fission; and the predominance of a particular process was a function of the relative development time scales. The internal Iribarren number (boundary slope/square root of wave slope) was found to be unable to categorize the breaking mechanisms, which were separable in wave slope versus boundary slope space. The breaking location was modelled in agreement with Helfrich (1992) over an extended parameter range and was independent of the Reynolds number (Re_w). The reflection coefficient at the beginning of the slope (R) was in agreement with the Bourgault & Kelley (2007) parameterization but increased by $\sim$10 % when Re_w was increased by a factor of 32. On the other hand, the breaking point reflection coefficient (R_b) could be up to $2R$ for mild slopes. The breaking mechanism was also Reynolds number dependent with a global instability occurring for the larger Re_w case.

While these conclusions suggest that laboratory-scale simulations do not capture large Re_w dynamics and hence that field-scale simulations are required, such simulations must be done with caution. Flow separation along the bottom boundary during breaking was found to be a mechanism controlling process and consequently the vertical grid point resolution must be sufficient to resolve the no-slip bottom boundary condition. Moreover, to correctly capture the turbulent dynamics and mixing efficiency, Fringer & Street (2003, their figure 17) have shown that transverse three-dimensional secondary instabilities must also be resolved, although large eddy scale simulations would probably be sufficient. Given the associated computational challenges, a combined approach of investigation using multiple scales and dimensions remains the appropriate path forward.

The authors thank Peter Diamessis for comments on boundary-layer separation and global instability and Karan Venayagamoorthy for discussions on internal bolus formation. Three anonymous reviewers are thanked for their constructive and valuable comments. The research was funded by NSERC Discovery Grants to L.B. and K.G.L. and by Queen's University. Kevin Hall is also thanked for financial support and encouragement.

REFERENCES

Apel, J. R. 2002 Oceanic internal waves and solitons. In *An Atlas of Oceanic Internal Solitary Waves*, Global Ocean Associates. Prepared for Office of Naval Research (Code 322 PO), 1-40.

Apel, J. R., Holbrook, J. R., Liu, A. K. & Tsai, J. J. 1985 The Sulu Sea internal soliton experiment. *J. Phys. Oceanogr.* **15**, 1625–1651.

Boegman, L., Imberger, J., Ivey, G. N. & Antenucci, J. P. 2003 High-frequency internal waves in large stratified lakes. *Limnol. Oceanogr.* **48**, 895–919.

Boegman, L. & Ivey, G. N. 2009 Flow separation and resuspension beneath shoaling nonlinear internal waves. *J. Geophys. Res.* **114**, C02018.

Boegman, L., Ivey, G. N. & Imberger, J. 2005 The degeneration of internal waves in lakes with sloping topography. *Limnol. Oceanogr.* **50**, 1620–1637.

Bogucki, D. J. & Redekopp, L. G. 1999 Global instability of separated flows: a paradigm for sediment resuspension by internal waves. *Geophys. Res. Lett.* **26**, 1317–1320.

Bogucki, D. J. Redekopp, L. G. & Barth, J. 2005 Internal solitary waves in the coastal mixing and optics 1996 experiment: multimodal structure and re-suspension. *J. Geophys. Res.* **110**, C02024.

Bourgault, D., Blokhina, M. D., Mirshak, R. & Kelley, D. E. 2007 Evolution of a shoaling internal solitary wave train. *Geophys. Res. Lett.* **34**, L03601.

Bourgault, D. & Kelley, D. 2003 Wave-induced boundary mixing in a partially mixed estuary. *J. Marine Res.* **61**, 553–567.

Bourgault, D. & Kelley, D. 2007 On the reflectance of uniform slopes for normally incident interfacial solitary waves. *J. Phys. Oceanogr.* **37**, 1156–1162.

Carr, M. & Davies, P. A. 2006 The motion of an internal solitary wave of depression over a fixed bottom boundary in a shallow, two-layer fluid. *Phys. Fluids* **18**, 016601.

Carr, M., Davies, P. A. & Shivaram, P. 2008 Experimental evidence of internal solitary wave-induced global instability in shallow water benthic boundary layers. *Phys. Fluids* **20**, 066603.

Dean, R. G. & Dalrymple, R. A. 1991 Water wave mechanics for engineers and scientists. In *Advanced Series on Ocean Engineering* (ed. L.-F. Liu), vol 2. World Scientific.

Diamessis, P. & Redekopp, L. G. 2006 Numerical investigation of solitary internal wave-induced global instability in shallow water benthic boundary layers. *J. Phys. Oceanogr.* **36**, 784–812.

Fringer, O. B. & Street, R. L. 2003 The dynamics of breaking progressive interfacial waves. *J. Fluid Mech.* **494**, 319–353.

Fructus, D., Carr, M., Grue, J., Jensen, A. & Davies, P. A. 2009 Shear-induced breaking of large internal solitary waves. *J. Fluid Mech.* **620**, 1–29.

Grimshaw, R., Pelinovsky, E. & Talipova, T. 1998 Solitary wave transformation due to a change in polarity. *Stud. Appl. Math.* **101**, 357–388.

Helfrich, K. R. 1992 Internal solitary wave breaking and run-up on a uniform slope. *J. Fluid Mech.* **243**, 133–154.

Helfrich, K. R., Melville, W. K. & Miles, J. W. 1984 On interfacialsolitary waves over slowly varying topography. *J. Fluid Mech.* **149**, 305–317.

Helfrich, K. R. & Melville W. K. 1986 On long nonlinear internal waves over slope-shelf topography. *J. Fluid Mech.* **167**, 285–308.

Horn, D. A., Imberger, J. & Ivey, G. N. 2001 The degeneration of large-scale interfacial gravity waves in lakes. *J. Fluid Mech.* **434**, 181–207.

Hosegood, P., Bonnin, J. & van Haren, H. 2004 Solibore-induced sediment resuspension in the Faeroe–Shetland Channel. *Geophys. Res. Lett.* **31**, L09301.

Hult, E. L., Troy, C. D. & Koseff, J. R. 2009 The breaking of interfacial waves at a submerged bathymetric ridge. *J. Fluid Mech.* **637**, 45–71.

Imberger, J. 1998 Flux path in a stratified lake. In *Physical Processes in Lakes and Oceans, Coastal and Estuarine Studies* (ed. J. Imberger), vol. 54, pp. 1–17. American Geophysical Union.

Jackson, C. 2007 Internal wave detection using the Moderate Resolution Imaging Spectroradiometer (MODIS). *J. Geophys. Res.* **112**, C11012.

Kao, T. W., Pan, F. S. & Renouard, D. 1985 Internal solitons on the pycnocline: generation, propagation and shoaling and breaking over a slope. *J. Fluid Mech.* **159**, 19–53.

Ledwell, J. R. & Hickey, B. M. 1995 Evidence for enhanced boundary mixing for the Santa Monica basin. *J. Geophys. Res.* **100** (20), 20665–20679.

Lamb, K. G. 1994 Numerical experiments of internal wave generation by strong tidal flow across a finite amplitude bank edge. *J. Geophy. Res.* **99**, 843–864.

Lamb, K. G. 2002 A numerical investigation of solitary internal waves with trapped cores formed via shoaling. *J. Fluid Mech.* **451**, 109–144.

Lamb, K. G., Boegman, L. & Ivey, G. N. 2005 Numerical simulations of shoaling internal solitary waves in tilting tank experiments. In *Proceedings of the 9th European Workshop on Physical Processes in Natural Waters*, pp. 31–38. Lancaster University.

Lamb, K. G. 2007 Energy and pseudoenergy flux in the internal wave field generated by tidal flow over topography. *Cont. Shelf Res.* **27**, 1208–1232.

Lamb, K. G. & Nguyen, V. T. 2009 Calculating energy flux in internal solitary waves with an application to reflectance. *J. Phys. Oceanogr.* **39**, 559–580.

Lamb, K. G. & Wan, B. 1998 Conjugate flows and flat solitary waves for a continuously stratified fluid. *Phys. Fluids.* **10**, 2061–2079.

Legg, S. & Adcroft, A. 2003 Internal wave breaking at concave and convex continental slopes. *J. Phys. Oceanogr.* **33**, 2224–2246.

Lorke, A. 2007 Boundary mixing in the thermocline of a large lake. *J. Geophys. Res.* **112**, C09019.

Marti, C. L. & Imberger, J. 2004 Exchange processes between littoral and pelagic waters in a stratified lake. *Mećanica Comput.* **23**, 1261–1274.

Michallet, H. & Ivey, G. N. 1999 Experiments on mixing due to internal solitary waves breaking on uniform slopes. *J. Geophys. Res.* **104**, 13467–13477.

Moum, J. N., Farmer, D. M., Smyth, W. D., Armi, L. & Vagle, S. 2003 Structure and generation of turbulence at interfaces strained by internal solitary waves propagating shoreward over the continental shelf. *J. Phys. Oceanogr.* **33**, 2093–2112.

Orr, M. H., & Mignerey, P. C. 2003 Nonlinear internal waves in the South China Sea: observation of the conversion of depression internal waves to elevation internal waves. *J. Geophys. Res.* **108**, C3, 3064.

Osborne, A. R., & Burch, T. L. 1980 Internal solitons in the Andaman Sea. *Science* **208**, 451–60.

Peregrine, D. H. 1983 Breaking waves on beaches. *Annu. Rev. Fluid Mech.* **15**, 149–178.

Shroyer, E. L., Moum, J. N. & Nash, J. D. 2009 Observations of polarity reversal in shoaling nonlinear internal waves. *J. Phys. Oceanogr.* **39**, 691–701.

Smyth, W. D. & Peltier, W. R. 1990 Three-dimensional primary instabilities of a stratified dissipative, parallel flow. *Geophys. Astrophys. Fluid Dyn.* **52**, 249–261.

Stastna, M. & Lamb, K. G. 2008 Sediment resuspension mechanisms associated with internal waves in coastal waters. *J. Geophys. Res.* **113**, C10016.

Sveen, J. K., Guo, Y., Davies, P. A. & Grue, J. 2002 On the breaking of internal solitary waves at a ridge. *J. Fluid Mech.* **469**, 161–188.

Talipova, T. G., Pelinovskii, E. N. & Grimshaw, R. 1997 Transformation of a soliton at appoint of zero nonlinearity. *Am. Inst. Phys. JETP Lett.* **65**, 120–125.

Thorpe, S. A. 1998 Some dynamical effects of internal waves and the sloping sides of lakes. In *Physical Processes in Lakes and Oceans*, *Coastal and Estuarine Studies* (ed. J. Imberger), vol. 54, pp. 441–460. American Geophysical Union.

Troy, C. D. & Koseff, J. R. 2005 The instability and breaking of long internal waves. *J. Fluid Mech.* **543**, 107–136.

Venayagamoorthy, S. K. & Fringer. O. B. 2007 On the formation and propagation of nonlinear internal boluses across a shelf break. *J. Fluid Mech.* **577**, 137–159.

Vlasenko, V. & Hutter, K. 2002 Numerical experiments on the breaking of solitary internal waves over a slope-shelf topography. *J. Phys. Oceanogr.* **32** (6), 1779–1793.

Vlasenko, V. & Stashchuk, N. 2007 Three-dimensional shoaling of large-amplitude internal waves. *J. Geophys. Res.* **112**, C11018.

Wüest, A., Piepke, G. & Van Senden, D. C. 2000 Turbulent kinetic energy balance as a tool for estimating vertical diffusivity in wind-forced stratified waters. *Limnol. Oceanogr.* **45**, 1388–1400.

Zhao, Z., Klemas, V. V., Zheng, Q. & Yan, X-H. 2003 Satellite observation of internal solitary waves converting polarity. *Geophys. Res. Lett.* **30**, 19.